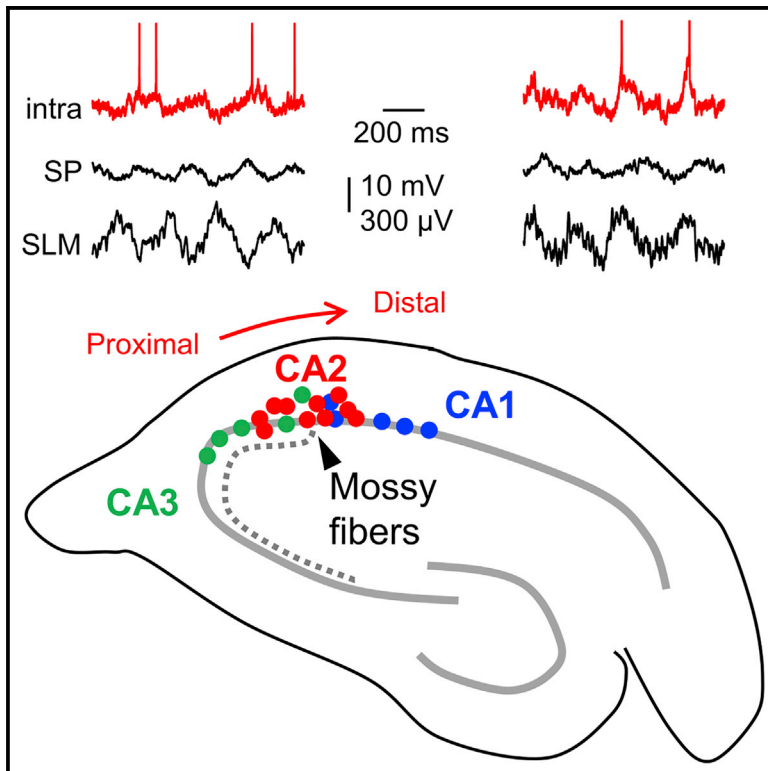Article

Proximodistal Organization of the CA2 Hippocampal Area

Graphical Abstract

Authors

Ivan Fernandez-Lamo,
Daniel Gomez-Dominguez,
Alberto Sanchez-Aguilera, ..., Elena Cid,
Antal Berenyi, Liset Menendez de la Prida

Correspondence

lmprida@cajal.csic.es

In Brief

The CA2 region of the hippocampus has distinctive molecular, physiological, and connectivity properties. Fernandez-Lamo et al. provide data supporting a proximodistal functional organization of this region in the rat.

Highlights

- The CA2 region is organized around the limit of the mossy fibers

- Heterogeneous pyramidal cell types populate the proximal and distal CA2 region

- Responses to intra- and extra-hippocampal inputs segregate along this axis

- CA2 oscillatory activity and spatial coding change proximodistally

CellPress

Proximodistal Organization of the CA2 Hippocampal Area

Ivan Fernandez-Lamo,[1,4] Daniel Gomez-Dominguez,[1,4] Alberto Sanchez-Aguilera,[1,4] Azahara Oliva,[2]
Aixa Victoria Morales,[1] Manuel Valero,[1] Elena Cid,[1] Antal Berenyi,[3] and Liset Menendez de la Prida[1,5,*]
[1]Instituto Cajal, CSIC, Ave Doctor Arce 37, Madrid 28002, Spain
[2]Department of Neuroscience, Zuckerman and Kavli Institutes, Columbia University, 3227 Broadway, New York, NY 10027, USA
[3]MTA-SZTE "Momentum" Oscillatory Neuronal Networks Research Group, Interdisciplinary Excellence Centre, Department of Physiology, University of Szeged, Szeged 6720, Hungary
[4]These authors contributed equally
[5]Lead Contact
*Correspondence: lmprida@cajal.csic.es
https://doi.org/10.1016/j.celrep.2019.01.060

SUMMARY

The proximodistal axis is considered a major organizational principle of the hippocampus. At the interface between the hippocampus and other brain structures, CA2 apparently breaks this rule. The region is involved in social, temporal, and contextual memory function, but mechanisms remain elusive. Here, we reveal cell-type heterogeneity and a characteristic expression gradient of the transcription factor Sox5 within CA2 in the rat. Using intracellular and extracellular recordings followed by neurochemical identification of single cells, we find marked proximodistal trends of synaptic activity, subthreshold membrane potentials, and phase-locked firing coupled to theta and gamma oscillations. Phase-shifting membrane potentials and opposite proximodistal correlations with theta sinks and sources at different layers support influences from different current generators. CA2 oscillatory activity and place coding of rats running in a linear maze reflect proximodistal state-dependent trends. We suggest that the structure and function of CA2 are distributed along the proximodistal hippocampal axis.

INTRODUCTION

The cornu ammonis 2 (CA2) hippocampal region has distinctive molecular, physiological, and connectivity properties (Dudek et al., 2016). CA2 pyramidal cells respond vigorously to direct entorhinal inputs from layer II stellate cells (Leroy et al., 2017; Sun et al., 2017). In addition, they receive a direct mossy fiber connection from granule cells and contribute to a parallel trisynaptic circuit to deep CA1 sublayers (Kohara et al., 2014; Sun et al., 2017). Recurrently associated with CA3, CA2 pyramidal cells project to superficial layers of the medial entorhinal cortex (Rowland et al., 2013). γ-Aminobutyric acid-ergic (GABAergic) innervation by local parvalbumin-expressing cells and specific classes of dendritic-targeting interneurons is particularly prominent in this region (Botcher et al., 2014; Mercer et al., 2012a,

2012b), supporting strong inhibitory control (Chevaleyre and Siegelbaum, 2010; Piskorowski and Chevaleyre, 2013). CA2 is specifically targeted by hypothalamic fibers releasing vasopressin and oxytocin during social interaction (Caldwell et al., 2008; Cui et al., 2013; Smith et al., 2016) and by supramammillary glutamatergic cells with a major role in wake-sleep regulation (Pedersen et al., 2017; Soussi et al., 2010).

Given recurrent connections with these brain systems, CA2 can be considered a network hub. Not surprisingly, it is involved in a diversity of functions, including spatial and social memory. Place fields are more abundant but less precise in CA2 than in CA3 and CA1 (Oliva et al., 2016a). Some studies have revealed that CA2 ensemble firing changes prominently over time (Alexander et al., 2016; Lee et al., 2015; Lu et al., 2015; Mankin et al., 2015). In contrast, others have reported some cells firing in place during brief exploratory pauses and over sleep (Kay et al., 2016). This leads to the idea that CA2 is specialized in bridging contextual representations, supporting their contribution to episodic memory function (Mankin et al., 2015; Wintzer et al., 2014). When CA2 cells are specifically manipulated, defects emerge in contextual habituation to a neutral environment (Boehringer et al., 2017), but not for contextual fear memory or spatial learning (Hitti and Siegelbaum, 2014). Instead, memory for a familiar conspecific is affected. Such a social memory role may reflect not only specific features of CA2 (Leroy et al., 2017) but also downstream effects (Okuyama et al., 2016; Raam et al., 2017). Possibly, CA2 is instrumental in interfacing among brain systems, but the mechanisms are not known.

The heterogeneous oscillatory behavior of putative CA2 cells was reported using extracellular recordings (Kay et al., 2016; Oliva et al., 2016b, 2016a). Moreover, in evaluating proximodistal changes of firing similarity between contexts, a significant spatial in-homogeneity was found at the CA3a-CA2 border (Lu et al., 2015). Unfortunately, without morphological confirmation, it is difficult to interpret these results given the miscellaneous composition of this transitional area (Valero et al., 2015). Here, we reveal striking heterogeneity of cell-type-specific molecular markers around dorsal CA2 in rats and use intracellular and extracellular in vivo recordings followed by neurochemical identification to target this region. We found marked proximodistal trends of synaptic activity and theta/gamma oscillations in both subthreshold membrane potentials and phase-locked
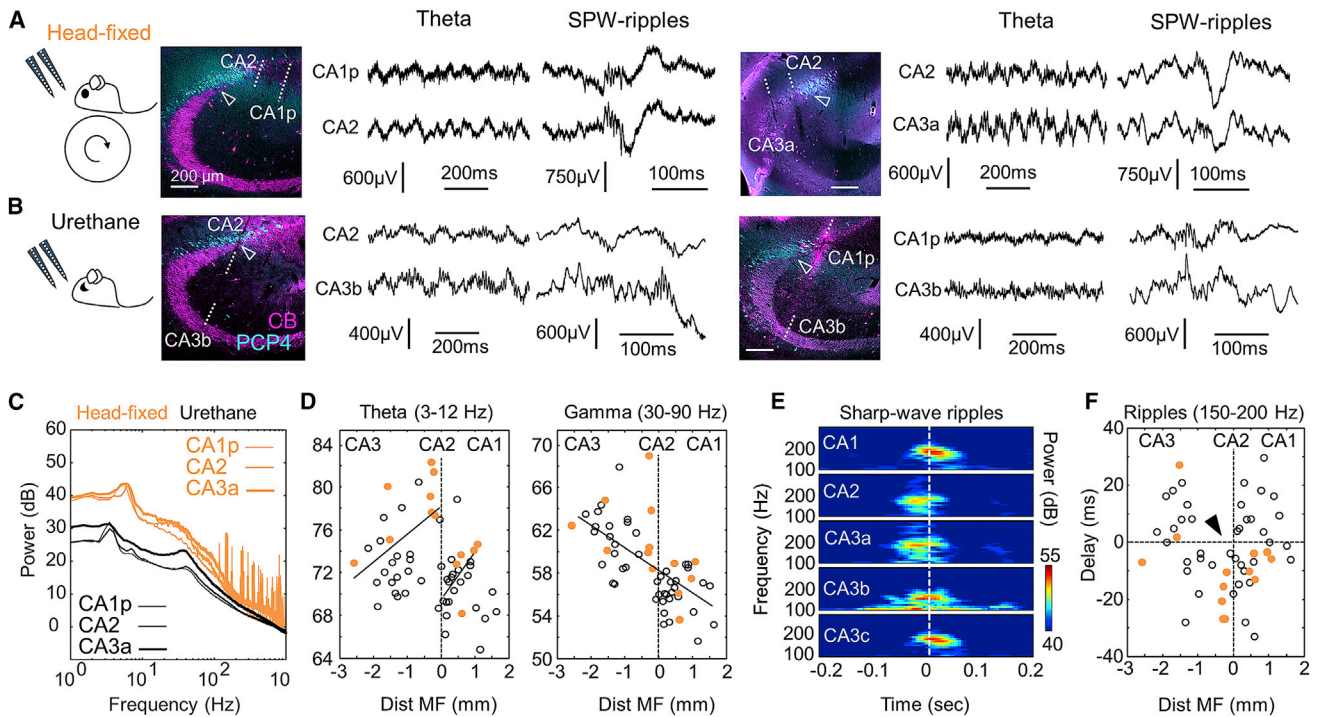
Figure 1. Characteristic Features of Local Field Potentials around CA2

(A) Representative simultaneous LFP signals recorded at SP in awake head-fixed rats using multisite silicon probes. Probe tracks are identified in sections immunostained against PCP4 and CB. The limit of MF (open arrowhead) is taken as a reference for quantitative analysis.

(B) LFP recordings around CA2 obtained from urethane anesthetized rats.

(C) Representative power spectra during theta activity recorded at SP of CA2, CA3a, and CA1p under urethane (black) and in head-fixed conditions (orange).

(D) Individual spectral area of the theta band (3–12 Hz) and the gamma band (30–90 Hz) plotted as a function of electrode distance to MF. Data are from 52 recording locations from n = 30 urethane anesthetized rats and 13 recordings from n = 5 drug-free rats. Different Pearson correlations were obtained at both sides of MF for theta: R = 0.47, p = 0.0059 from −3 to 0 mm and R = 0.59, p = 0.0088 from 0 to 1 mm. Gamma power exhibited a significant negative correlation (R = −0.65, p < 0.0001).

(E) Grand average spectra of the ripple power recorded at SP (aligned by the sharp-wave peak at SR).

(F) Delay between the ripple power peak and the sharp-wave peak as a function of recording location. Note the earlier ripple peak (negative delays) at the limit with MF (arrowhead).

See also Figure S1.

firing. Our data disclose opposing entrainment by different current generators and GABAergic microcircuits across the proximal and distal sectors. Moreover, we found that these trends shape CA2 pyramidal cell state-dependent oscillatory activity and place coding.

RESULTS

Characteristic Features of Local Field Potentials around CA2

Local field potentials (LFPs) were recorded with multisite silicon probes around CA2 in 5 awake head-fixed rats. To target CA2 precisely, we learned to identify characteristic evoked responses to stimulation of the ipsilateral perforant pathway (PP) and contralateral CA3 (Figures S1A–S1D) (STAR Methods). Theta oscillations and sharp-wave ripples were recorded during periods of running and immobility, respectively.

In simultaneous recordings from the stratum pyramidale (SP), we noted attenuation of theta activity and characteristic sharp-

wave ripple patterns around the CA2-CA1 border, as identified by the specific marker PCP4 (Figure 1A, left). Immunostaining against calbindin (CB) helped us to delineate the point at which mossy fibers (MFs) terminate (Figure 1A, arrowhead). Theta-nested gamma oscillations were typically recorded from CA3 (Figure 1A, right). Similar LFP profiles were recorded under urethane in 30 rats (Figure 1B), despite spectral differences with the drug-free condition (Figure 1C).

We evaluated LFP features quantitatively using detailed information on the location of recording sites along SP with respect to anatomical borders. The spectral power of the theta band (3–12 Hz) and the gamma band (30–90 Hz) was plotted as a function of the site distance to MF along the SP contour (n = 13 recordings from 5 awake head-fixed rats, n = 52 recordings from 30 anesthetized rats) (Figure 1D) (STAR Methods). We noted representative spatial in-homogeneities of LFP signals around CA2. For theta, positive Pearson correlations were confirmed at both sides of the MF limit in an otherwise-negative global trend (Figure 1D, left; see also Figures S1E and S1F). This correlation

paradox (Julious and Mullee, 1994) was not present in the gamma power, which decreased consistently (Figure 1D, right). We also confirmed characteristic features of sharp-wave ripples around CA2 by looking at the temporal relationship between the ripple power and the sharp-wave peak (Figure 1E). As described (Oliva et al., 2016b), the maximal ripple power preceded sharp-wave peaks at CA2 (Figure 1F; Figures S1G and S1H). Independent of whether these features reflect volume-conducted and/or microcircuit effects, they represent characteristic LFP signatures of the CA2 region.

Molecular and Electrophysiological Cell-Type-Specific Heterogeneity around CA2

We next characterized cellular diversity around CA2. Immunoreactivity against PCP4, α-Actinin2, CB, and Wfs1 allowed for classification of different cell types (STAR Methods). Using the MF limit as a natural morphological landmark, we defined the proximal and distal sectors of CA2 (Figure 2A, discontinuous line), corresponding to CA2a and CA2b subregions (Dudek et al., 2016). We noted many cells positive for PCP4 distributed at both sides of the MF limit in rats (Figure 2A), in contrast to mice that exhibit a narrower distal CA2 (Figure 2B) (Dudek et al., 2016; Kohara et al., 2014). We also noted some PCP4+ cells in deep layers of CA3a in both species (Figures 2A and 2B, arrowheads). Similar to CA2 cells, they co-expressed PCP4 and α-Actinin2 (Figure S2A). Many Wfs1+ CA1 pyramidal cells interspersed with α-Actinin2+ cells at distal CA2 (Figure 2A, right). According to our estimates, CA2 spans about 250 μm around the MF limit in the rat dorsal hippocampus (bregma −2.9 to −3.7 mm).

Using VGAT-VenusA transgenic rats to exclude interneurons, we quantified the distribution of pyramidal cells with cell-type-specific immunostaining (Figure S2B). Double immunostaining against α-Actinin2/PCP4 (n = 6 sections from 3 rats) and α-Actinin2/Wfs1 (n = 6 sections from 3 rats) supported cellular heterogeneity within CA2 (Figure 2C). At proximal CA2, most cells were PCP4+/α-Actinin2+ (∼65%), and some were negative for both markers (∼15%). These cells were VGAT−, indicating they had a glutamatergic phenotype. In double immunostaining against α-Actinin2/Wfs1, we found a minority of Wfs1+ cells at proximal CA2 (<5%). In contrast, at distal CA2, many Wfs1+/α-Actinin2− cells (∼35%) intermingled with α-Actinin2+ cells (50%). The remaining Wfs1−/α-Actinin2− cells were VGAT+. Thus, heterogeneous cell types intermix with CA2 pyramidal cells at the proximal and distal sectors. Similar features were seen in coronal and sagittal sections, confirming they did not depend on the orientation.

To identify cell types more precisely, we obtained *in vivo* intracellular recordings in urethane anesthetized rats, in combination with 16-channel silicon probes (Figure 2D). We targeted pyramidal cells around the CA2 region using characteristic LFP features to guide sharp electrode penetrations (Figure S1B). After recordings, cells were filled with Neurobiotin, visualized with streptavidin, and tested against PCP4, α-Actinin2, Wfs1, and CB immunoreactivity. Cell morphology was examined at 63× magnification under the confocal microscope to look for thorny excrescences typical of CA3 pyramidal cells.

A total of 24 pyramidal cells were impaled in 24 rats. We found n = 5 α-Actinin2− or PCP4− cells with thorny excrescences classified as CA3 cells (Figure 2D, green), n = 10 cells expressing PCP4 being classified as CA2 pyramidal cells (red), and n = 9 Wfs1+ CA1 pyramidal cells (blue). PCP4+ and Wfs1+ cells did not exhibit thorny excrescences. We recorded the proximodistal position of cell somata with respect to MF and confirmed the heterogeneous cellular composition of the CA2 region (Figure 2E). Electrophysiologically, we found no significant differences in the resting membrane potential (RMP), but we did find proximodistal trends for the maximal firing rate and sag in response to current pulses, confirmed by Pearson correlation (Figure 2E). We also noted some differences in the after-hyperpolarization (AHP) following an action potential (Figure 2E). Some of these features were described *in vitro* for CA3a and CA2 pyramidal cells (Srinivas et al., 2017; Sun et al., 2017). While differences in input resistance and difficulties to evaluate intrinsic properties *in vivo* may complicate interpretation, data suggest interaction between cell type and proximodistal location (Table S1).

We next looked for markers that may help in further identifying a proximodistal axis within CA2. Regionalized gene expression has been described along the transverse hippocampal axis and is exploited to define borders between regions along the *Cornu Ammonis* (Cembrowski et al., 2016). While working with Sox5, a transcription factor involved in several aspects of neuronal development, including cell fate determination (Quiroga et al., 2015), we noted increasing proximodistal expression along CA3-CA2 in adult mice (Figures S2C and S2D). This region- and cell-type-specific trend was cross-validated using RNA sequencing (RNA-seq) mouse data from Hipposeq (Cembrowski et al., 2016) (Figure S2E). In rats, we found a similar gradient of Sox5 expression (Figure 2F; Figure S2F) and confirmed regional trends by segmenting SP along CA3a-CA2 (one-way ANOVA, F(24) = 4.7, p = 0.008) (Figure 2G). Next, we asked whether Sox5 was differentially expressed across single cells within CA2 using co-localization with α-Actinin2 (Figure 2H, top). Quantification of the mean intensity of Sox5 expression in α-Actinin2+ cells showed a characteristic maximum around the point at which MF terminate (Figure 2H, bottom). Consistently, the expression dynamics of Sox5 reversed around this point, as tested separately at proximal and distal sectors (Figures 2H and 2I). Thus, in addition to different cell-type heterogeneity at proximal and distal sectors, the CA2 pyramidal cell population exhibits proximodistal molecular gradients around the MF border.

Cell-Type-Specific Differences of Theta and Gamma Firing Modulation around CA2

Next, we asked for functional proximodistal variations. Intracellular recordings obtained simultaneously to multisite LFP signals allowed us to evaluate oscillatory behavior of identified cell types around CA2 (n = 24 cells) (Figures 3A and 3B). Juxtacellularly labeled cells recorded simultaneously to LFPs in awake head-fixed rats were also obtained (n = 3 cells) (Figures 3B and 3C) (STAR Methods). Although theta under urethane (∼4 Hz) may differ from running theta (6–8 Hz), we aimed to compare modulatory influences across and within cell types.
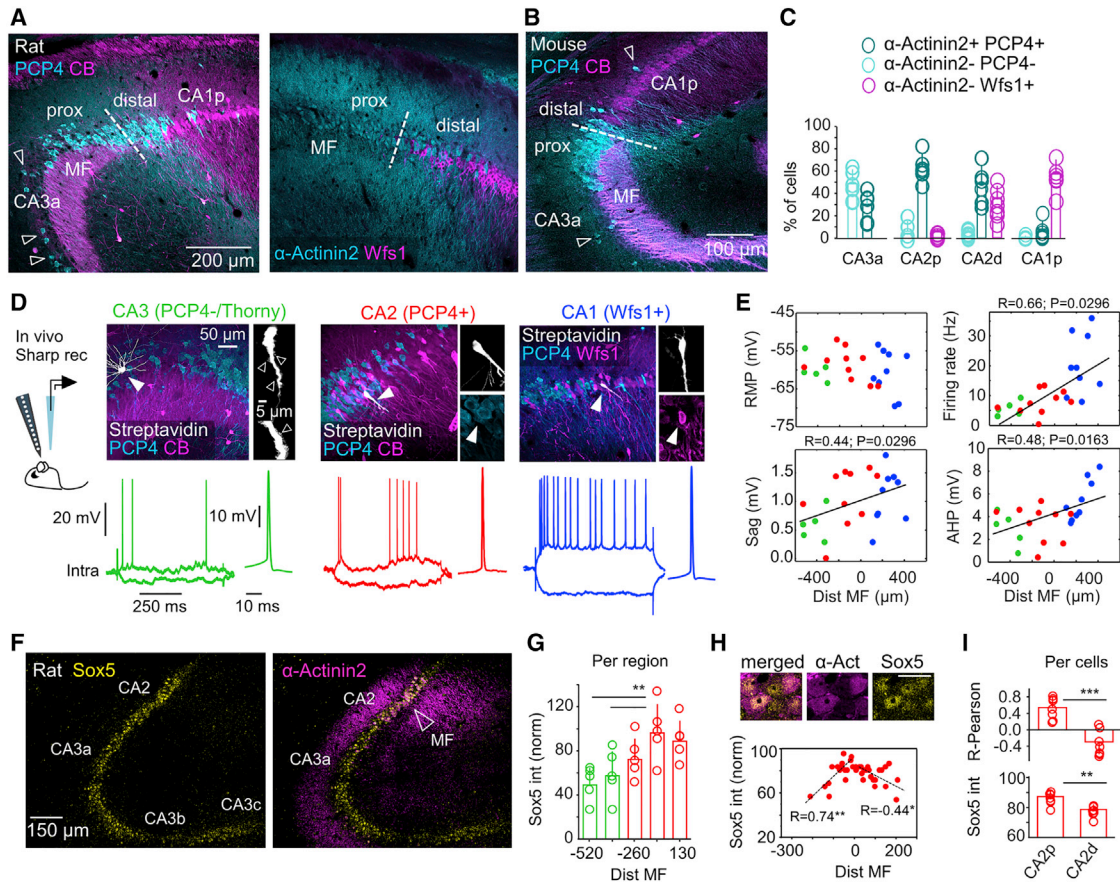
Figure 2. Cell-Type-Specific Heterogeneity around CA2

(A) Immunoreactivity against PCP4, α-Actinin2, CB, and Wfs1 allowed evaluating cell-type heterogeneity around CA2. Images show co-localization among different markers (3 confocal optical sections). Some PCP4+ cells were identified in deep layers of CA3a and in CA1 (open arrows). MF was used to define the proximal (close to CA3a) and distal (close to CA1) sectors of CA2.

(B) PCP4 and CB expression in the mouse CA2.

(C) Quantification of pyramidal cell types around CA2, as examined in double immunostaining against α-Actinin2/PCP4 (n = 6 sections from 3 rats) and α-Actinin2/Wfs1 (n = 6 sections from 3 rats). Individual data points are shown, together with mean ± SD.

(D) Intracellular recordings of CA2 pyramidal cells obtained *in vivo* from urethane anesthetized rats. Cells with thorny excrescences (open arrowheads) and lacking immunoreactivity for PCP4 or α-Actinin2 were classified as CA3 (green, n = 5). Cells positive to Wfs1 either CB+ or CB− were classified as CA1 (blue, n = 9). Cells immunoreactive to PCP4 or α-Actinin2 without thorny excrescences were classified as CA2 cells (red, n = 10).

(E) Intrinsic properties of the different cell types plotted as a function of their distance to MF. Proximodistal gradients were confirmed by a Pearson correlation, as indicated. Intrinsic properties were measured at the resting membrane potential (RMP). Sag and firing rate were calculated in response to ±0.3 nA current pulses. AHP was calculated from the first spike in response to +0.2 nA.

(F) Immunohistochemical expression of Sox5 in a representative section of the rat dorsal hippocampus co-localized with α-Actinin2 (1 confocal section).

(G) Quantification of Sox5 expression per region (normalized by background at 0) along the proximodistal axis of CA3 to CA2 (n = 5 sections from 4 rats). Significant one-way ANOVA, $F_{(24)} = 4.7$, $p = 0.008$. Post hoc Tukey test, **$p < 0.001$. Error bars show mean ± SD.

(H) Expression of Sox5 in CA2 cells as a function of the cell distance to MF (1 confocal section). A Pearson correlation R index was evaluated for proximal (−250 to 0 μm) and distal (0 to 250 μm) sectors separately. *$p < 0.05$, **$p < 0.001$. One representative section is shown.

(I) Mean group data (±SD) of the Pearson correlation and mean normalized intensity for proximal and distal CA2 cells. Data from n = 7 sections from 4 rats. Paired Student's (two-tailed) t tests, **$p < 0.01$, ***$p < 0.0001$.

See also Figure S2 and Table S1.

Under urethane, the power spectrum of intracellular membrane potential oscillations suggested a significant proximodistal gradient of the gamma power (30–90 Hz), but not the theta power (4–12 Hz) (with similar trends for slow and fast gamma bands: R = −0.61, p = 0.0014, and R = −0.67, p = 0.0003, respectively) (Figures 3D and 3E). Phase-locked firing of single cells to LFP signals from the stratum lacunosum moleculare (SLM) exhibited opposite behavior for theta and gamma (Figure 3F). Theta-firing modulation increased toward distal CA2, while gamma modulation reversed, as quantified by the mean vector length (MVL) (Figure 3G). For this analysis, we included juxtacellularly labeled cells, which fit into the distribution (Figure 3G, open dots). We noted a separated cluster of poorly theta-modulated cells, especially some distal Wfs1+ and

PCP4+ cells (Figure 3G, arrowheads), resembling spatial LFP inhomogeneities.

Given the deep-superficial gradients reported in CA1 and CA2 (Oliva et al., 2016b; Valero et al., 2015), we looked for the distribution of modulatory strength as a function of the cell distance within SP. We found significant correlation with the deep-superficial position for gamma modulation of all cells together and within the PCP4+ group alone (superficial is at 0) (Figure 3H). A different modulatory index, looking for pairwise phase consistency (PPC) (Vinck et al., 2012), captured similar correlations (Figures S3A and S3B). Comparable effects were seen for the slow and fast gamma bands separately (Figure S3C). However, because of the typical expansion of the cell layer around CA2, the deep-superficial and proximodistal axes may interact. A generalized linear model (GLM) accounting for cell types and proximodistal and deep-superficial influences confirmed interactions (Table S2).

Cells recorded around CA2 exhibited phase-locked firing (z = 6.3, p = 0.0049, Rayleigh test) (Figure 3I). Significant proximodistal gradients of the preferred theta phase were confirmed with circular-linear statistics (R = 0.78, p < 0.0001, for all cells and R = 0.63, p = 0.0348, for CA2 cells alone) (Figure 3I). No statistical effects were found as a function of deep-superficial location (Figure 3J). These results did not depend on proximodistal differences of LFP signals caused by penetrations of the silicon probe along CA2 to CA1 (no correlation with probe position; Table S2).

Altogether, our data suggest CA2 firing is organized proximodistally during theta oscillations. Considering the reversal profile of theta cycles around SP of CA1, our data suggest proximal PCP4+ pyramidal cells tend to fire along the falling phase, together with CA3 cells, while distal cells fire in phase with CA1 pyramidal cells near the theta trough (Figure 3K). Thus, firing from CA2 pyramidal cells consistently shifts in phase from proximal to distal. Complex mechanisms accounting for these functional effects could include local microcircuit factors and the influence of different theta generators (Figure 3L).

CA2 Pyramidal Cells May Couple to Different Proximodistal Theta Generators

We sought to evaluate the contribution of different mechanisms with additional analysis. We focused on n = 10 PCP4+ CA2 cells recorded intracellularly to avoid cell-type effects. We examined membrane oscillations at different holding potentials during theta recorded extracellularly (Figure 4A). Current source density (CSD) signals allowed identification of theta-associated local transmembrane sinks and sources (Figure 4A, color map) (STAR Methods). Theta current generators were localized at the stratum oriens (SO), stratum radiatum (SR), and SLM layers as described previously (Montgomery et al., 2009).

The frequency of intracellular theta oscillations was independent of the holding potential (Figure 4A), but the oscillatory power reached a minimum between −80 and −60 mV in different cells (Figure 4B, arrowhead). For a given cell, the intracellular theta power depicted a characteristic U-shaped curve with minimal power potential (Figure 4C). When plotted as a function of the cell position with respect to MF, the minimal power potential exhibited a significant proximodistal correlation for all PCP4+ cells

(no deep-superficial correlation, p = 0.79) (Figure 4D). This minimal power potential reflects the equilibrium potential for mixed excitatory and inhibitory synaptic drives contributing to intracellular oscillations (Soltesz and Deschênes, 1993) and suggests proximodistal trends of theta currents. At RMP, the phase of intracellular oscillatory peaks showed a significant proximodistal shift with respect to LFP (Figure 4E). Thus, CA2 pyramidal cells experienced different theta current drives along the proximodistal axis, with depolarizing peaks consistently shifting in phase from proximal (Figure 4Fa) to distal (Figure 4Fb).

To complement this analysis, we chose only those PCP4+ cells recorded simultaneously to CA2 extracellular LFPs (n = 5). By evaluating coherence between intracellular membrane potential and local CSD signals, we aimed to quantify the influences of transmembrane currents at different strata during theta oscillations. We also included in this analysis one CA3 cell and one Wfs1+ CA1 pyramidal cell recorded simultaneously to LFP signals from CA2 to control for cell-type-specific effects. To circumvent issues arising from the complex hippocampal geometry, we limited the analysis to penetrations going through SO, SR, and SLM of distal CA2 (Figure 4A, inset). One PCP4+ cell was excluded due to the more proximal location of SLM penetration.

We found opposing proximodistal correlations between intracellular theta oscillations and CSD signals at SO and SR for all cells and for PCP4+ cells alone (Figure 4G), suggesting that transmembrane currents flowing though basal and apical dendrites contributed differently along the proximodistal axis. Moreover, correlation between intracellular and local CSD signals at SLM was significant only for PCP4+ pyramidal cells (Figure 4G, bottom), consistent with their responsiveness to entorhinal inputs (Srinivas et al., 2017; Sun et al., 2017).

Different Proximodistal Influences of Intra- and Extra-hippocampal Inputs to CA2

Next, we examine microcircuit determinants of proximodistal gradients within CA2 with stimulation of input pathways in vivo (Figure 5A). Intracellular synaptic responses were evaluated at different latencies in current-clamp configuration for paired-pulse stimulation of the contralateral CA3 (n = 20 cells) and ipsilateral entorhinal inputs (n = 12 cells). Responses to electrical stimulation of entorhinal inputs were validated optogenetically (Figure S1B).

We found no proximodistal trends for the amplitude of excitatory postsynaptic potentials (EPSPs) but found significant correlation for di-synaptic inhibitory postsynaptic potentials (IPSPs) in response to contralateral CA3 stimulation (Figure 5B, upper plots). For entorhinal inputs, we noted clear EPSP responses only in PCP4+ cells (Figure 5B, lower plots), consistent with our results on theta coherence and previous data in vitro (Srinivas et al., 2017; Sun et al., 2017). Mean group responses per cell type reflected these differences (Figure 5C). An inhibitory/excitatory (I/E) ratio confirmed cell-type differences (also for the excitatory/inhibitory [E/I] ratio, data not shown) (Figure 5D). No effect was found for paired-pulse stimulation.

To exclude cell-type-specific effects and to examine synaptic currents more precisely, we performed voltage-clamp patch-clamp recordings in vitro (Figure 5E, left) (STAR Methods). Cells in the vicinity of CA2 were recorded and filled with Alexa 568 for
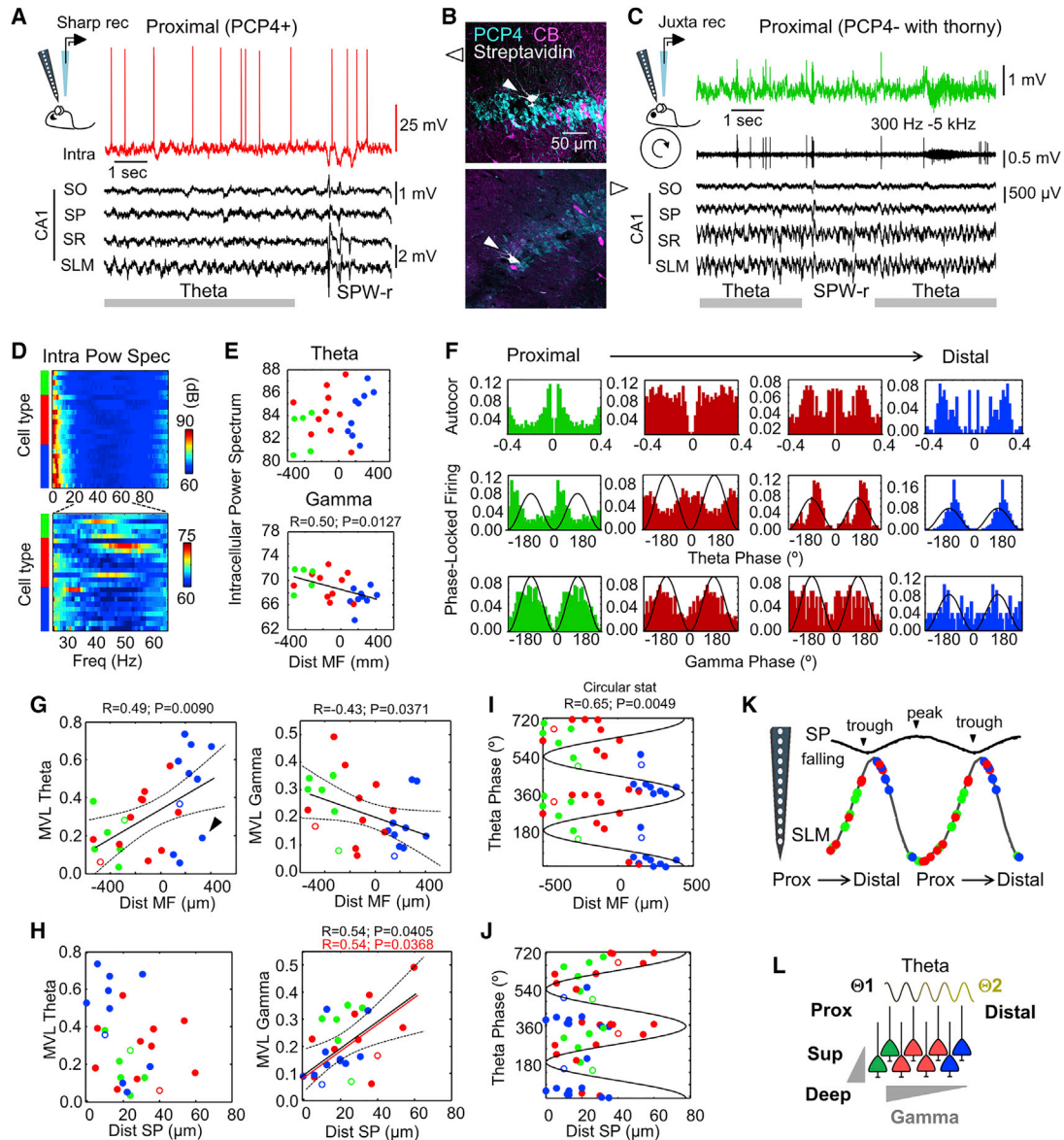
Figure 3. Proximodistal Differences of Theta and Gamma Activity of CA2 Pyramidal Cells

(A) Intracellular recordings obtained simultaneously to multisite LFP signals allowed evaluation of oscillatory behavior of different cell types around CA2. Note the poor theta rhythmicity of spontaneous firing in a proximal PCP4+ CA2 cell but consistent phase-locking preference with theta cycles at SLM. Note also clear hyperpolarization during sharp-wave (SPW) ripples.

(B) Neurochemical classification of cells shown in (A) and (C).

(C) Single-cell and LFP recordings from head-restrained rats.

(D) Power spectrum of the intracellular membrane potential recorded during LFP theta in different cell types. Cells are ranked according to their proximodistal location within each group. Data from n = 5 CA3 cells (green), n = 10 CA2 cells (red), and n = 9 CA1 cells (blue).

(E) Individual single-cell data of theta and gamma power of membrane potential oscillations.

(F) Representative examples of single-cell autocorrelation and phase-locking firing to theta and gamma waves recorded at SLM. Cells are ranked according to their proximodistal location.

(G) Proximodistal distribution of the modulatory strength for theta and gamma for cells recorded under urethane (filled circles; 24 cells) and in drug-free conditions (open circles; 3 cells). The discontinuous line indicates the 95% confidence interval. Note the separate cluster of poorly modulated cells (arrowhead).

(H) Distribution of the modulatory strength as a function of the cell distance within SP (0 is the superficial limit).

(I) Theta phase firing preference of single cells measured against the SLM signal. The circular distribution significance is indicated.

(J) Theta phase firing preference of cells plotted as a function of their deep-superficial location.

(K) Phase firing preference of single cells represented against the CA1 SP signal (note the reversal of the theta wave along the CA1 layers).

(L) Potential mechanisms may include proximodistal and deep-superficial microcircuit organization and the influence of different theta generators.

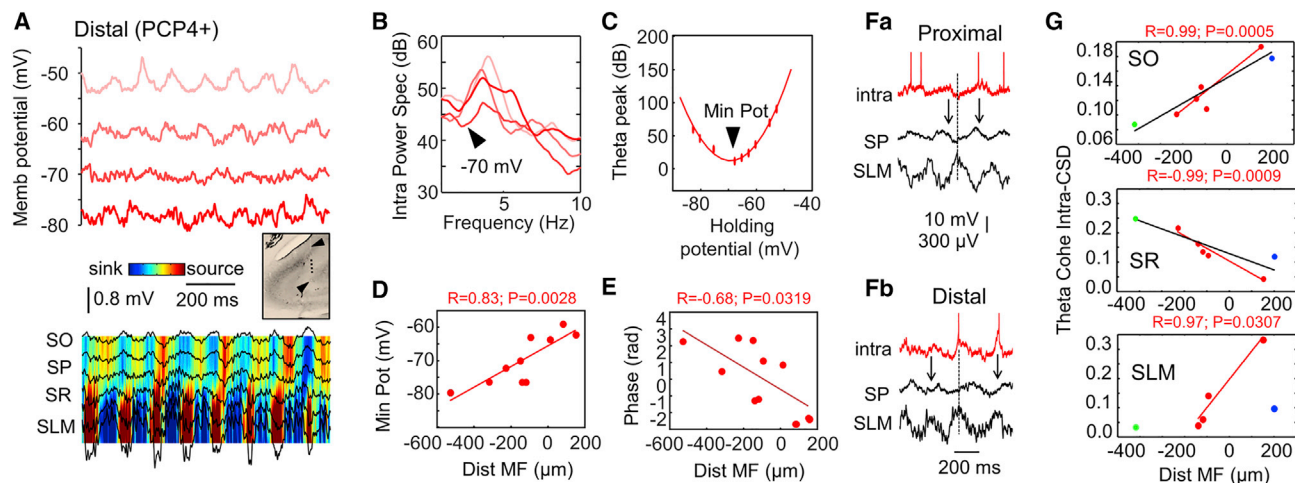See also Figure S3 and Table S2.

Figure 4. Influence of Different Proximodistal Theta Drives along CA2

(A) Intracellular membrane oscillations recorded at different holding potentials simultaneously to extracellular LFP signals in one PCP4+ pyramidal cell. CSD local sinks and sources are shown, together with LFPs (color map). Note attenuated theta oscillations around −70 mV in this cell, near the reversal potential of γ-aminobutyric acid a (GABAa) receptors. LFP and CSD signals were recorded simultaneously to the −70 mV trace. The inset shows validation of probe penetration through the distal CA2 region.

(B) Power spectrum of membrane potential oscillations of traces shown in (A). Note the reduced theta power for a holding potential near −70 mV.

(C) Relationship between theta power of membrane potential oscillations and holding potential for the cell shown in A. A minimum theta power is estimated at −70 mV (arrowhead). The thick line shows the best polynomial fit.

(D) Significant gradients of minimal power potential along the proximodistal axis. Data from n = 10 PCP4+ CA2 cells.

(E) Phase relationship between the membrane oscillation peak at RMP and the proximodistal location of CA2 cells.

(F) Example of a proximal PCP4+ CA2 cell (a). Note the maximal depolarization and firing at the falling phase of theta recorded at SP. Example of a distal cell (b) with maximal depolarization and firing at the SP theta trough. In both cases, LFP signals were recorded from the distal CA2.

(G) Proximodistal distribution of theta coherence between membrane potential oscillations at RMP and the local CSD signal at SO, SR, and SLM from the distal CA2 region. Data from cells recorded simultaneously to CA2 extracellular LFP signals (n = 1 CA3, n = 5 CA2, n = 1 CA1). In one CA2 cell, the SLM CSD signal did not meet the inclusion criteria.

neurochemical identification. Evoked excitatory postsynaptic currents (EPSCs) and inhibitory postsynaptic currents (IPSCs) were evaluated in response to CA3 and SLM stimulation (Figure 5E, right). We confirmed similar population responses for electrical and optogenetic stimulation of SLM (Figure S1D). In a preliminary set of experiments, we noted a significant effect of recording duration and access resistance in immunoreactivity against PCP4+, presumably due to cell dialysis (Figure S4). Thus, we reduced patching time to the minimum to gain in neurochemical characterization. Cells were tested first against PCP4 and subsequently for Wfs1. Cells without thorny excrescences and negative to both markers were left unclassified.

Consistent with *in vivo* data, we found significant trends for the amplitude of IPSCs upon stimulation of CA3 for all cells and within PCP4+ cells alone (Figure 5F, no difference for EPSCs; Figure S5A) (n = 7 PCP4+, n = 8 Wfs1+, n = 6 not-confirmed cells). The I/E ratio reflected similar global correlation with the cell distance to MF (Figure 5F, similar trends for E/I: R = 0.34, p = 0.0081; Figure S5C, left). The frequency of spontaneous IPSCs measured in all cells, but not that of EPSCs, exhibited significant proximodistal correlation (Figure 5G; Figure S5D).

In contrast, responses to entorhinal inputs at SLM were more complex. First, we found significant proximodistal trends for the EPSC amplitude only in PCP4+ cells (n = 7 PCP4+, n = 6 Wfs1+, n = 7 not-confirmed cells) (Figure 5H, left) and no differences for IPSCs (Figure S5B). Second, an I/E ratio showed opposing corre-

lations for PCP4+ CA2 and Wfs1+ CA1 pyramidal cells around the MF limit (Figure 5H, right, similar for the E/I ratio; Figure S5C, right). We found no clear evidence of deep-superficial gradients in synaptic potentials along CA2 in response to either pathway (Figure S6). Finally, we confirmed previous reports of cell-type-specific responses to MF stimulation (Sun et al., 2017), with smaller EPSCs in PCP4+ CA2 cells compared with CA3a cells (Figure S7). Thus, our data support different influences from input pathways along CA2. Accordingly, different intra-hippocampal (e.g., CA3) and extra-hippocampal (e.g., entorhinal cortex) theta current generators (Buzsáki, 2002; Montgomery et al., 2009) may influence CA2 cells along the proximodistal axis (Figure 5I).

Proximodistal Differences of Oscillatory Activity and Spatial Coding of CA2 Cells

We reasoned that a proximodistal distribution of CA2 activity should be reflected in functional operations within this hippocampal region. To investigate this point, we looked at data on large-scale simultaneous recordings of pyramidal cells from the CA3a, CA2, and proximal CA1 regions in rats during spatial navigation in a linear maze and subsequent sleep (Oliva et al., 2016a). We identified 6 rats with penetrations at different proximodistal locations along CA2 (Figure 6A). A total of 688 pyramidal cells were sorted (387 from rats 6, 7, and 8 at proximal locations and 301 from rats 2, 4, and 5 at distal locations). Theta signals recorded from the CA1 SLM served as reference.
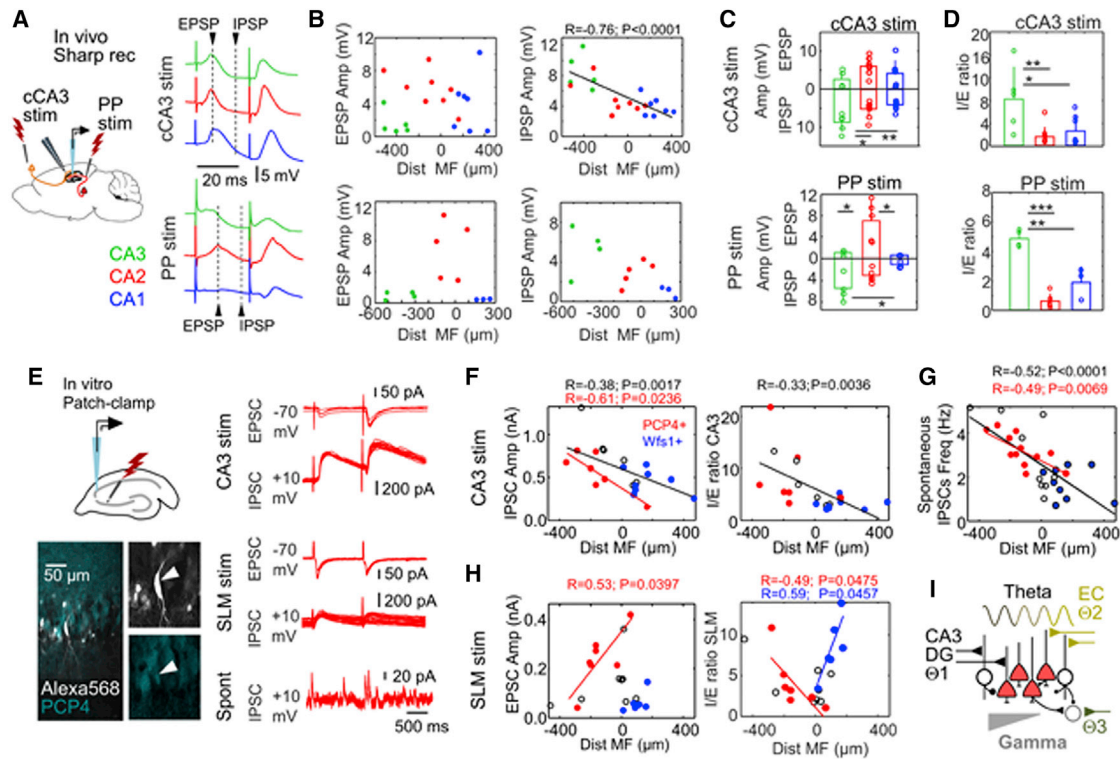
Figure 5. Proximodistal Gradients of Synaptic Responses along CA2

(A) Intracellular responses to contralateral CA3 (cCA3) and PP stimulation were examined *in vivo*. The amplitudes of evoked EPSPs and IPSPs were evaluated at different latencies from stimulation (arrowheads). Cell types are identified by colors.

(B) Synaptic responses to cCA3 stimulation (n = 20 cells) and PP stimulation (n = 12 cells). Data are plotted as a function of the cell distance to MF.

(C) Mean group responses (±SD) and individual data per cell type. Because of their location, cell-type differences reflect a proximodistal gradient along CA2. cCA3 stimulation: EPSP is non-significant; IPSP F(19) = 9.1, p = 0.011, one-way ANOVA; *p < 0.05, **p < 0.005, post hoc Tukey test. PP stimulation: EPSP F(11) = 8.9, p = 0.007; IPSP F(11) = 6.1, p = 0.021; *p < 0.05, post hoc Tukey test.

(D) I/E ratio of different cell types. cCA3 stimulation: F(19) = 6.5, p = 0.008, one-way ANOVA; *p < 0.05, **p < 0.005, post hoc Tukey test. PP simulation: F(11) = 41.1, p < 0.0001; **p < 0.005, ***p < 0.0001, post hoc Tukey test.

(E) *In vitro* recordings were obtained to evaluate synaptic currents in response to CA3 or SLM stimulation. Cells were filled with Alexa 568 for posterior identification. Evoked excitatory postsynaptic currents (EPSCs) and inhibitory postsynaptic currents (IPSCs) from the PCP+ pyramidal cell are shown.

(F) Synaptic currents evoked by CA3 stimulation. Wfs1+ CA1 cells (n = 8) and PCP4+ CA2 cells (n = 7) are shown in blue and red, respectively. Cells not confirmed neurochemically are indicated in black (n = 6). Significant proximodistal trend for IPSC and the I/E ratio are indicated.

(G) Spontaneous IPSC frequency from n = 12 PCP4+, n = 9 Wfs1+, and n = 9 not confirmed.

(H) Synaptic currents evoked by stimulation of entorhinal inputs at SLM (n = 7 PCP4+ CA2 cells, n = 6 Wfs1+ CA1 cells, n = 7 not-confirmed cells).

(I) Schematic representation of a proximodistal microcircuit organization of CA2. Intra-hippocampal (CA3 and dentate gyrus [DG]) and extra-hippocampal input pathways (entorhinal cortex [EC] and possibly septum or the supramammillary nucleus) relay different theta current generators at different layers along the proximodistal axis of CA2. Local GABAergic inputs also exhibit a proximodistal distribution, consistent with gamma oscillations.

See also Figures S4–S7.

Consistent with data reported above, the preferred theta phase of CA2 pyramidal cells shifted along the proximodistal axis during both running (RUN) and rapid-eye-movement (REM) sleep (Figure 6B) (data from each rat shown independently). A one-way ANOVA confirmed proximodistal trends across cell types (RUN: F = 25.4, p < 0.0001; REM: F = 22.5, p < 0.0001) (Figure 6C). No difference of theta modulation was detected around CA2 (Figure 6D); however, neurons in CA3b and CA3c regions were found in an earlier study to be slightly more phase locked to theta (Oliva et al., 2016b). During RUN, we found stronger cross-correlations between firing from proximal CA2 and firing from CA3a pyramidal cells (p = 0.0111), whereas distal CA2 cells were better correlated with CA1p pyramidal cells (p = 0.0303) (Figure 6E). During REM

sleep, firing of proximal and distal CA2 pyramidal cells was differently modulated by slow (30–60 Hz) and fast (60–90 Hz) gamma (Figure 6F). The proximodistal trend for the slow gamma band was consistent with data shown earlier under urethane. Finally, we also examined whether place coding properties distributed differently across the proximodistal axis in CA2. As reported earlier, spatially modulated CA2 pyramidal cells from the proximal and distal sectors may exhibit more than one place field (Figure 6G). We found more spatially modulated cells with larger selectivity and carrying more information content per spike at distal than at proximal sectors (Figure 6H). Altogether, these data support different state-dependent oscillatory dynamics and place coding along the proximodistal axis in CA2.
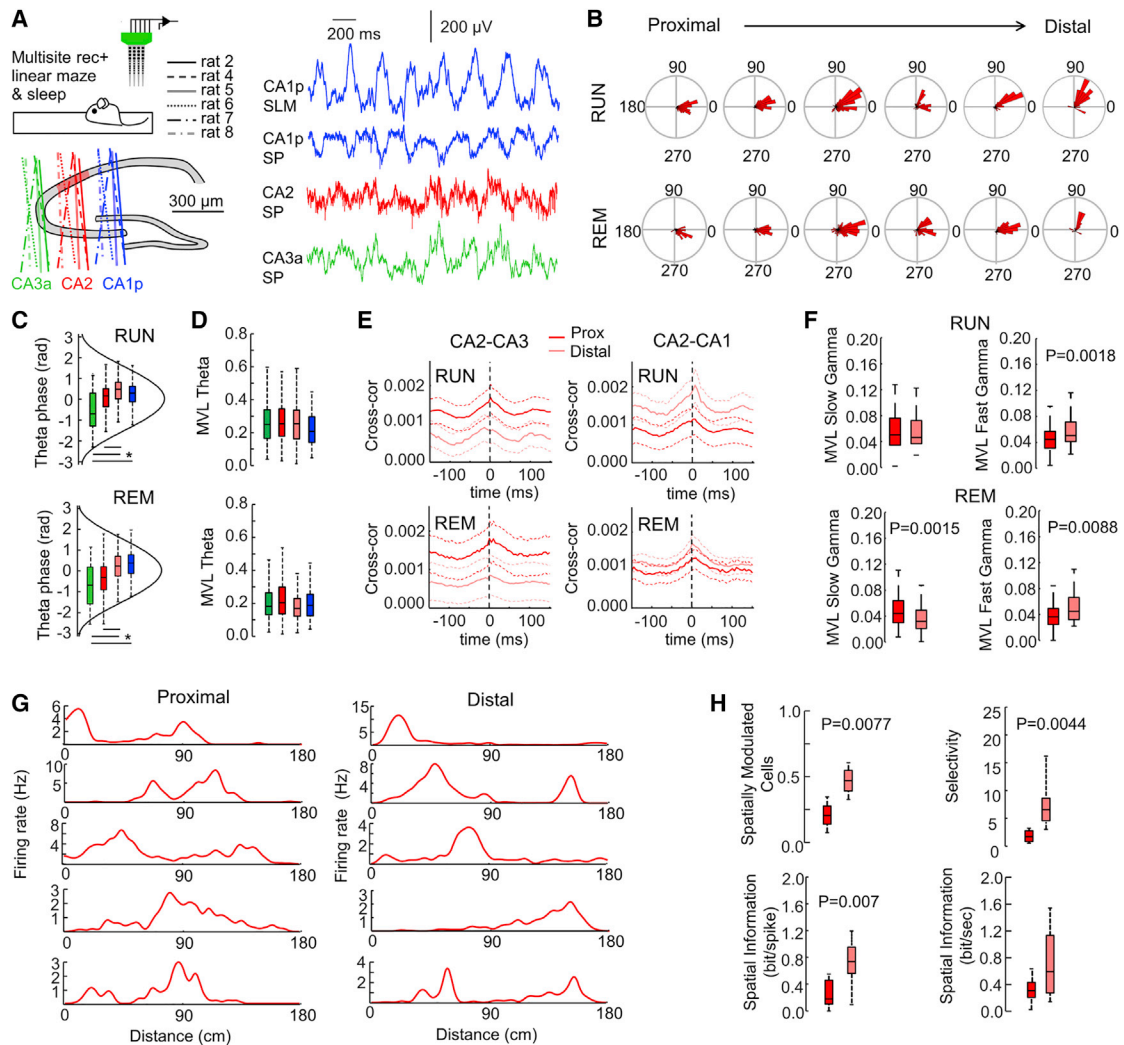
Figure 6. Proximodistal Organization of CA2 Activity in Time and Space

(A) High-density multisite silicon probes (256 channels) allowed simultaneous recordings of CA3, CA2, and CA1 unit activity from 6 rats running (RUN) in a linear maze and subsequently sleeping (REM) (Oliva et al., 2016a).

(B) Mean theta phase modulation from pyramidal cells from the 6 rats organized from proximal to distal penetrations through CA2. A total of 688 CA2 pyramidal cells were isolated: 87 from rat 2, 126 from rat 4, 88 from rat 5, 65 from rat 6, 188 from rat 7, and 134 from rat 8. The reference for theta cycles was taken at SLM of CA1, with the theta peak at zero. Data from RUN and REM episodes are shown separately.

(C) Proximodistal group difference of the preferred theta phase for RUN (F = 25.4, p < 0.0001) and REM (F = 22.5, p < 0.0001). Note the statistical differences for proximal and distal CA2. Data are from 262 pyramidal cells in CA3a, 387 pyramidal cells in proximal CA2, 301 pyramidal cells in distal CA2, and 389 pyramidal cells in proximal CA1. *p < 0.05 from post hoc t test.

(D) No statistical effects were found between groups in the strength of theta modulation.

(E) Cross-correlation between pyramidal cells from proximal and distal CA2 with CA3 and with CA1. Proximal CA2 neuronal firing is more correlated with CA3 firing, whereas distal CA2 cells tend to better correlate with CA1, especially during RUN periods. Data are shown as mean ± SEM.

(F) Proximodistal differences of slow and fast gamma modulation.

(G) Representative examples of CA2 place cells recorded from the proximal and distal sectors.

(H) Proximodistal differences of spatial coding properties of CA2 place cells.

DISCUSSION

Our data suggest that within CA2, opposite influences from different input pathways and local gradients of the E/I ratio shape neuronal firing. Intra-hippocampal inputs from CA3 (and dentate gyrus [DG]) converge proximally to modulate CA2 pyramidal cell firing in phase with CA3a cells during theta oscillations. In contrast, at distal sectors, extra-hippocampal activity operates maximally at SO and SLM to shift CA2 pyramidal cell firing toward CA1. Proximodistal effects on CA2 oscillatory activity operate differently across states (awake, REM sleep, and urethane). The depth of theta modulation increases toward distal CA2

under urethane, while slow and fast gamma influences are differentially modulated during REM sleep. CA2 place cells exhibited different selectivity along the proximodistal axis. Therefore, the CA2 output dissociates proximodistally in the dorsal hippocampus of the rat.

The transverse axis is central to hippocampal function. Initially identified in single CA3 pyramidal cells projecting to CA1 (Ishizuka et al., 1990; Li et al., 1994), a proximodistal topography quickly emerged as a major organizational principle of intra-hippocampal connectivity (Witter et al., 2000). Proximal CA3c cells (near DG) project distally to CA1, whereas distal CA3a project proximally. Analogous connectivity was identified for the CA1 projections to subiculum, where strong proximodistal gradients support functional dissociation (Amaral and Witter, 1989; Cembrowski et al., 2018). The medial and lateral entorhinal inputs separate proximodistally in CA1 (Witter et al., 2000), and this is reflected in the organization of place fields (sharper at proximal CA1 and unspecific at distal CA1) (Henriksen et al., 2010). Similar functional segregation is present at CA3 (Lu et al., 2015). Given differences in recurrent connectivity (Ishizuka et al., 1990; Li et al., 1994), the ability of the CA3 network to separate patterns degrades toward CA3a, where more recurrent collaterals favor pattern completion (Lee et al., 2015).

Using PCP4, α-Actinin2, and Wfs1 as cell-type-specific markers, we found sharply organized variations of cellular composition around the CA2 transitional region. CA3a and CA1 pyramidal cells interspersed distinctly in CA2 at the proximal and distal sectors. Yet they all retain their different input preferences with intra- and extra-hippocampal inputs. The transcription factor Sox5 showed a marked proximodistal expression from CA3 to CA2, consistent with transcriptomic variability among hippocampal cell types (Cembrowski et al., 2016). However, Sox5 also reflects proximodistal variabilities within CA2 pyramidal cells, with distal cells expressing lower levels of Sox5 compared with proximal cells and a sharp inflection gradient at the point where MFs terminate. This is consistent with the idea of distinct functionalities emerging from graded genetic variations (Cembrowski and Menon, 2018) and supports molecular heterogeneity within CA2. Sox5 is not likely to characterize CA2 cells specifically; rather, it appears to correlate with the functional organization around the MF border. Inter-species differences of CA2 may arise around this border as noted previously (Dudek et al., 2016).

Our electrophysiological data reveal that different proximodistal microcircuits determine functional properties within CA2 pyramidal cells as well. Distal CA2 cells receive stronger entorhinal inputs and lower di-synaptic inhibition in response to both CA3 and PP stimulation. We found that during spontaneous theta activity, the peak and reversal of membrane potential oscillations shifted in phase, consistent with different phase-locking preferences at proximal and distal sectors. Other report also noted different theta modulation in pyramidal cells recorded around CA2 in mouse, but neurochemical confirmation was not available (Matsumoto et al., 2016). Three independent analyses provided additional support to this functional distribution along the transverse axis. First, somatic membrane potential oscillations were more influenced by SLM and SO theta currents in distal CA2 cells, whereas proximal cells

followed SR currents. Given the known layered organization of entorhinal, septal, and supramammillary inputs at SLM and SO (Joshi et al., 2017; Soussi et al., 2010), our data suggest distal CA2 cells may be more biased toward extra-hippocampal theta generators, while proximal CA2 cells may follow intra-hippocampal influences (Buzsáki, 2002; Montgomery et al., 2009). Proximodistal differences of I/E balance and distinctive plasticity properties of different pathways may further contribute (Dasgupta et al., 2017; Leroy et al., 2017; Nasrallah et al., 2017; Piskorowski and Chevaleyre, 2013; Sun et al., 2017).

A second observation reinforced the idea of a proximodistal distribution of CA2 function. Gamma activity, particularly slow gamma (30–60 Hz), interfered largely with theta in proximal cells, as confirmed in both subthreshold membrane potential oscillations and neuronal firing. A confounding deep-superficial trend interacted with proximodistal variations of feedforward inhibition, possibly reflecting diverse interneuronal connectivity (Botcher et al., 2014; Mercer et al., 2012a, 2012b). These data do not contradict previous findings of strong inhibition around CA2 (Chevaleyre and Siegelbaum, 2010; Piskorowski and Chevaleyre, 2013; Valero et al., 2015); they just support a proximodistal organization along the transverse axis, consistent with other reports (Sun et al., 2017). Axons from bistratified CA2 interneurons are shown to arborize distally, while SP-SR interneurons innervate locally in proximal CA2 and CA3a (Mercer et al., 2012a, 2012b). All these complex interactions along the transverse axis, together with volume-conduction effects, may contribute to characteristic LFPs around CA2. While the gamma power measured at SP consistently decreased, theta power exhibited a strong in-homogeneity at the point where MF terminates. In addition, parallel extracellular dipoles from interspersed CA3a and CA1 pyramidal cells will contribute distinctly to LFP signals. Possibly, MF inputs recruiting preferentially CA3 versus CA2 cells (Kohara et al., 2014; Sun et al., 2017) and SLM inputs doing the opposite (Srinivas et al., 2017) will reinforce geometrical asymmetries in the area. Ripples preceding the local sharp-wave peak in proximal locations strengthen the idea of complex local LFPs explained by microcircuit mechanisms (Oliva et al., 2016b; Valero et al., 2015).

Finally, large-scale recording of pyramidal cells with high-density silicon probes confirmed relevant proximodistal trends within CA2 in rats RUN in a linear maze and during subsequent REM sleep. In this independent dataset (Oliva et al., 2016a, 2016b), we found distribution similar to that in urethane for the preferred theta phase in the proximal and distal CA2 region during RUN and REM sleep. These gamma modulatory influences segregated during sleep, with proximal CA2 cells experiencing stronger modulation by slow gamma and distal CA2 cells exhibiting stronger influences by fast gamma. Given the pathway dependency of slow and fast theta-gamma coupling, this suggests different control of spike timing of proximal and distal CA2 cells by CA3a and entorhinal inputs (Fernández-Ruiz et al., 2017). The opposite trends of firing cross-correlation between proximal and distal CA2 cells with CA3a and CA1p, together with the more spatial selectivity of distal CA2 cells, support this view.

Spatial and non-spatial memories, as well as the ability for pattern separation, segregate along the transverse CA3-CA2 axis (Hunsaker et al., 2008; Lee et al., 2015; Nakamura et al.,

2013). Place field similarity between contexts changes abruptly 200–250 μm from the CA2 border (Lu et al., 2015). This fits perfectly with the proximal CA2 region, where PCP4+ cells fire in phase with CA3a. At this border, oxytocin receptor signaling plays a role in discriminating social stimuli (Raam et al., 2017). Given recurrent interactions between CA3a and CA2 pyramidal cells (Li et al., 1994; Wittner and Miles, 2007), a proximodistal integration of social and contextual information may be responsible for more flexible representations (DeVito et al., 2009; Pagani et al., 2015; Raam et al., 2017; Wintzer et al., 2014). In contrast, distal CA2 cells fired in phase with proximal CA1 pyramidal neurons and a lower I/E balance suggest different computational operations compared with the proximal sector (Guzman et al., 2016; Sun et al., 2017). Our findings that distal CA2 cells are more driven by entorhinal inputs and have stronger fast gamma modulation than proximal cells suggest the circuit can accommodate additional functionalities (Jones and McHugh, 2011; Valero and de la Prida, 2018). Social contexts can modify spatial fields in CA2 (Alexander et al., 2016), possibly due to cell-type-specific interactions (Kohara et al., 2014; Okuyama et al., 2016).

In summary, we propose that CA2 operates along the proximodistal axis, similar to other hippocampal regions, and that this segregation is critical to better understanding its functional role.

STAR★METHODS

Detailed methods are provided in the online version of this paper and include the following:

- KEY RESOURCES TABLE
- CONTACT FOR REAGENT AND RESOURCE SHARING
- EXPERIMENTAL MODEL AND SUBJECT DETAILS
- METHOD DETAILS
  - Juxtacellular and LFP recordings in head-fixed rats
  - Intracellular and LFP recordings under urethane
  - *In vitro* electrophysiology
  - Tissue processing and inmunohistochemistry
  - Analysis of Sox5 expression
  - Optogenetics
  - Analysis of LFP signals
  - Analysis of intracellular recordings
  - Analysis of juxtacellularly labeled cells
  - Analysis of large-scale recordings of pyramidal cells during RUN and sleep
- QUANTIFICATION AND STATISTICAL ANALYSIS
- DATA AND SOFTWARE AVAILABILITY

AUTHOR CONTRIBUTIONS

L.M.d.l.P. designed the study. I.F.-L., A.S.-A., E.C., M.V., A.O., A.B., and A.V.M. obtained data. D.G.-D., I.F.-L., A.S.-A., M.V., E.C., A.O., A.V.M., and L.M.d.l.P. analyzed and interpreted the data. L.M.d.l.P. wrote the paper.

DECLARATION OF INTERESTS

The authors declare no competing interests.

REFERENCES

Alexander, G.M., Farris, S., Pirone, J.R., Zheng, C., Colgin, L.L., and Dudek, S.M. (2016). Social and novel contexts modify hippocampal CA2 representations of space. Nat. Commun. *7*, 10300.

Amaral, D.G., and Witter, M.P. (1989). The three-dimensional organization of the hippocampal formation: a review of anatomical data. Neuroscience *31*, 571–591.

Boehringer, R., Polygalov, D., Huang, A.J.Y., Middleton, S.J., Robert, V., Wintzer, M.E., Piskorowski, R.A., Chevaleyre, V., and McHugh, T.J. (2017). Chronic loss of CA2 transmission leads to hippocampal hyperexcitability. Neuron *94*, 642–655.

Botcher, N.A., Falck, J.E., Thomson, A.M., and Mercer, A. (2014). Distribution of interneurons in the CA2 region of the rat hippocampus. Front. Neuroanat. *8*, 104.

Buzsáki, G. (2002). Theta oscillations in the hippocampus. Neuron *33*, 325–340.

Caldwell, H.K., Wersinger, S.R., and Young, W.S., 3rd. (2008). The role of the vasopressin 1b receptor in aggression and other social behaviours. Prog. Brain Res. *170*, 65–72.

Cembrowski, M.S., and Menon, V. (2018). Continuous variation within cell types of the nervous system. Trends Neurosci. *41*, 337–348.

Cembrowski, M.S., Wang, L., Sugino, K., Shields, B.C., and Spruston, N. (2016). Hipposeq: a comprehensive RNA-seq database of gene expression in hippocampal principal neurons. eLife *5*, e14997.

Cembrowski, M.S., Phillips, M.G., DiLisio, S.F., Shields, B.C., Winnubst, J., Chandrashekar, J., Bas, E., and Spruston, N. (2018). Dissociable structural and functional hippocampal outputs via distinct subiculum cell classes. Cell *173*, 1280–1292.

Chevaleyre, V., and Siegelbaum, S.A. (2010). Strong CA2 pyramidal neuron synapses define a powerful disynaptic cortico-hippocampal loop. Neuron *66*, 560–572.

Cui, Z., Gerfen, C.R., and Young, W.S., 3rd. (2013). Hypothalamic and other connections with dorsal CA2 area of the mouse hippocampus. J. Comp. Neurol. *521*, 1844–1866.

Dasgupta, A., Baby, N., Krishna, K., Hakim, M., Wong, Y.P., Behnisch, T., Soong, T.W., and Sajikumar, S. (2017). Substance P induces plasticity and synaptic tagging/capture in rat hippocampal area CA2. Proc. Natl. Acad. Sci. USA 114, E8741–E8749.

DeVito, L.M., Konigsberg, R., Lykken, C., Sauvage, M., Young, W.S., 3rd, and Eichenbaum, H. (2009). Vasopressin 1b receptor knock-out impairs memory for temporal order. J. Neurosci. 29, 2676–2683.

Dudek, S.M., Alexander, G.M., and Farris, S. (2016). Rediscovering area CA2: unique properties and functions. Nat. Rev. Neurosci. 17, 89–102.

Fernández-Ruiz, A., Oliva, A., Nagy, G.A., Maurer, A.P., Berényi, A., and Buzsáki, G. (2017). Entorhinal-CA3 dual-input control of spike timing in the hippocampus by theta-gamma coupling. Neuron 93, 1213–1226.

Guzman, S.J., Schlögl, A., Frotscher, M., and Jonas, P. (2016). Synaptic mechanisms of pattern completion in the hippocampal CA3 network. Science 353, 1117–1123.

Henriksen, E.J., Colgin, L.L., Barnes, C.A., Witter, M.P., Moser, M.B., and Moser, E.I. (2010). Spatial representation along the proximodistal axis of CA1. Neuron 68, 127–137.

Hitti, F.L., and Siegelbaum, S.A. (2014). The hippocampal CA2 region is essential for social memory. Nature 508, 88–92.

Hunsaker, M.R., Rosenberg, J.S., and Kesner, R.P. (2008). The role of the dentate gyrus, CA3a,b, and CA3c for detecting spatial and environmental novelty. Hippocampus 18, 1064–1073.

Ishizuka, N., Weber, J., and Amaral, D.G. (1990). Organization of intrahippocampal projections originating from CA3 pyramidal cells in the rat. J. Comp. Neurol. 295, 580–623.

Jones, M.W., and McHugh, T.J. (2011). Updating hippocampal representations: CA2 joins the circuit. Trends Neurosci. 34, 526–535.

Joshi, A., Salib, M., Viney, T.J., Dupret, D., and Somogyi, P. (2017). Behavior-dependent activity and synaptic organization of septo-hippocampal GABAergic neurons selectively targeting the hippocampal CA3 area. Neuron 96, 1342–1357.e5.

Julious, S.A., and Mullee, M.A. (1994). Confounding and Simpson's paradox. BMJ 309, 1480–1481.

Kay, K., Sosa, M., Chung, J.E., Karlsson, M.P., Larkin, M.C., and Frank, L.M. (2016). A hippocampal network for spatial coding during immobility and sleep. Nature 531, 185–190.

Kohara, K., Pignatelli, M., Rivest, A.J., Jung, H.-Y., Kitamura, T., Suh, J., Frank, D., Kajikawa, K., Mise, N., Obata, Y., et al. (2014). Cell type-specific genetic and optogenetic tools reveal hippocampal CA2 circuits. Nat. Neurosci. 17, 269–279.

Lee, H., Wang, C., Deshmukh, S.S., and Knierim, J.J. (2015). Neural population evidence of functional heterogeneity along the CA3 transverse axis: pattern completion versus pattern separation. Neuron 87, 1093–1105.

Leroy, F., Brann, D.H., Meira, T., and Siegelbaum, S.A. (2017). Input-timing-dependent plasticity in the hippocampal CA2 region and its potential role in social memory. Neuron 95, 1089–1102.

Li, X.-G., Somogyi, P., Ylinen, A., and Buzsáki, G. (1994). The hippocampal CA3 network: an in vivo intracellular labeling study. J. Comp. Neurol. 339, 181–208.

Lu, L., Igarashi, K.M., Witter, M.P., Moser, E.I., and Moser, M.B. (2015). Topography of place maps along the CA3-to-CA2 axis of the hippocampus. Neuron 87, 1078–1092.

Mankin, E.A., Diehl, G.W., Sparks, F.T., Leutgeb, S., and Leutgeb, J.K. (2015). Hippocampal CA2 activity patterns change over time to a larger extent than between spatial contexts. Neuron 85, 190–201.

Matsumoto, N., Okamoto, K., Takagi, Y., and Ikegaya, Y. (2016). 3-Hz subthreshold oscillations of CA2 neurons in vivo. Hippocampus 26, 1570–1578.

Mercer, A., Eastlake, K., Trigg, H.L., and Thomson, A.M. (2012a). Local circuitry involving parvalbumin-positive basket cells in the CA2 region of the hippocampus. Hippocampus 22, 43–56.

Mercer, A., Botcher, N.A., Eastlake, K., and Thomson, A.M. (2012b). SP-SR interneurones: a novel class of neurones of the CA2 region of the hippocampus. Hippocampus 22, 1758–1769.

Montgomery, S.M., Betancur, M.I., and Buzsáki, G. (2009). Behavior-dependent coordination of multiple theta dipoles in the hippocampus. J. Neurosci. 29, 1381–1394.

Nakamura, N.H., Flasbeck, V., Maingret, N., Kitsukawa, T., and Sauvage, M.M. (2013). Proximodistal segregation of nonspatial information in CA3: preferential recruitment of a proximal CA3-distal CA1 network in nonspatial recognition memory. J. Neurosci. 33, 11506–11514.

Nasrallah, K., Piskorowski, R.A., and Chevaleyre, V. (2017). Bi-directional interplay between proximal and distal inputs to CA2 pyramidal neurons. Neurobiol. Learn. Mem. 138, 173–181.

Okuyama, T., Kitamura, T., Roy, D.S., Itohara, S., and Tonegawa, S. (2016). Ventral CA1 neurons store social memory. Science 353, 1536–1541.

Oliva, A., Fernández-Ruiz, A., Buzsáki, G., and Berényi, A. (2016a). Spatial coding and physiological properties of hippocampal neurons in the cornu ammonis subregions. Hippocampus 26, 1593–1607.

Oliva, A., Fernández-Ruiz, A., Buzsáki, G., and Berényi, A. (2016b). Role of hippocampal CA2 region in triggering sharp-wave ripples. Neuron 91, 1342–1355.

Pagani, J.H., Zhao, M., Cui, Z., Avram, S.K., Caruana, D.A., Dudek, S.M., and Young, W.S. (2015). Role of the vasopressin 1b receptor in rodent aggressive behavior and synaptic plasticity in hippocampal area CA2. Mol. Psychiatry 20, 490–499.

Pedersen, N.P., Ferrari, L., Venner, A., Wang, J.L., Abbott, S.B.G., Vujovic, N., Arrigoni, E., Saper, C.B., and Fuller, P.M. (2017). Supramammillary glutamate neurons are a key node of the arousal system. Nat. Commun. 8, 1405.

Piskorowski, R.A., and Chevaleyre, V. (2013). Delta-opioid receptors mediate unique plasticity onto parvalbumin-expressing interneurons in area CA2 of the hippocampus. J. Neurosci. 33, 14567–14578.

Quiroga, A.C., Stolt, C.C., Diez del Corral, R., Dimitrov, S., Pérez-Alcalá, S., Sock, E., Barbas, J.A., Wegner, M., and Morales, A.V. (2015). Sox5 controls dorsal progenitor and interneuron specification in the spinal cord. Dev. Neurobiol. 75, 522–538.

Raam, T., McAvoy, K.M., Besnard, A., Veenema, A.H., and Sahay, A. (2017). Hippocampal oxytocin receptors are necessary for discrimination of social stimuli. Nat. Commun. 8, 2001.

Rowland, D.C., Weible, A.P., Wickersham, I.R., Wu, H., Mayford, M., Witter, M.P., and Kentros, C.G. (2013). Transgenically targeted rabies virus demonstrates a major monosynaptic projection from hippocampal area CA2 to medial entorhinal layer II neurons. J. Neurosci. 33, 14889–14898.

San Antonio, A., Liban, K., Ikrar, T., Tsyganovskiy, E., and Xu, X. (2014). Distinct physiological and developmental properties of hippocampal CA2 subfield revealed by using anti-Purkinje cell protein 4 (PCP4) immunostaining. J. Comp. Neurol. 522, 1333–1354.

Smith, A.S., Williams Avram, S.K., Cymerblit-Sabba, A., Song, J., and Young, W.S. (2016). Targeted activation of the hippocampal CA2 area strongly enhances social memory. Mol. Psychiatry 21, 1137–1144.

Soltesz, I., and Deschênes, M. (1993). Low- and high-frequency membrane potential oscillations during theta activity in CA1 and CA3 pyramidal neurons of the rat hippocampus under ketamine-xylazine anesthesia. J. Neurophysiol. 70, 97–116.

Soussi, R., Zhang, N., Tahtakran, S., Houser, C.R., and Esclapez, M. (2010). Heterogeneity of the supramammillary-hippocampal pathways: evidence for a unique GABAergic neurotransmitter phenotype and regional differences. Eur. J. Neurosci. 32, 771–785.

Srinivas, K.V., Buss, E.W., Sun, Q., Santoro, B., Takahashi, H., Nicholson, D.A., and Siegelbaum, S.A. (2017). The dendrites of CA2 and CA1 pyramidal neurons differentially regulate information flow in the cortico-hippocampal circuit. J. Neurosci. 37, 3276–3293.

Sun, Q., Sotayo, A., Cazzulino, A.S., Snyder, A.M., Denny, C.A., and Siegelbaum, S.A. (2017). Proximodistal heterogeneity of hippocampal CA3 pyramidal neuron intrinsic properties, connectivity, and reactivation during memory recall. Neuron *95*, 656–672.

Uematsu, M., Hirai, Y., Karube, F., Ebihara, S., Kato, M., Abe, K., Obata, K., Yoshida, S., Hirabayashi, M., Yanagawa, Y., and Kawaguchi, Y. (2008). Quantitative chemical composition of cortical GABAergic neurons revealed in transgenic venus-expressing rats. Cereb. Cortex *18*, 315–330.

Valero, M., and de la Prida, L.M. (2018). The hippocampus in depth: a sublayer-specific perspective of entorhinal-hippocampal function. Curr. Opin. Neurobiol. *52*, 107–114.

Valero, M., Cid, E., Averkin, R.G., Aguilar, J., Sanchez-Aguilera, A., Viney, T.J., Gomez-Dominguez, D., Bellistri, E., and de la Prida, L.M. (2015). Determinants of different deep and superficial CA1 pyramidal cell dynamics during sharp-wave ripples. Nat. Neurosci. *18*, 1281–1290.

Vinck, M., Battaglia, F.P., Womelsdorf, T., and Pennartz, C. (2012). Improved measures of phase-coupling between spikes and the local field potential. J. Comput. Neurosci. *33*, 53–75.

Wintzer, M.E., Boehringer, R., Polygalov, D., and McHugh, T.J. (2014). The hippocampal CA2 ensemble is sensitive to contextual change. J. Neurosci. *34*, 3056–3066.

Witter, M.P., Wouterlood, F.G., Naber, P.A., and Van Haeften, T. (2000). Anatomical organization of the parahippocampal-hippocampal network. Ann. N Y Acad. Sci. *911*, 1–24.

Wittner, L., and Miles, R. (2007). Factors defining a pacemaker region for synchrony in the hippocampus. J. Physiol. *584*, 867–883.

STAR★METHODS

KEY RESOURCES TABLE

REAGENT or RESOURCE	SOURCE	IDENTIFIER
Antibodies		
Rabbit anti-calbindin D-28k	Swant	Swant CB-38; RRID:AB_10000340
Mouse anti-calbindin D-28k	Swant	Swant 300; RRID:AB_10000347
Mouse anti-NeuN	Millipore	Cat# MAB377; RRID:AB_2298772
Rabbit anti-Wfs1	Proteintech	Cat# 11558-1-AP; RRID:AB_2216046
Mouse Anti-α-Actinin2	Sigma	Cat#: A-7811; RRID: AB_476766
Rabbit anti-PCP4	Sigma	Cat#: HPA5792; RRID: AB_1855086
Mouse anti-Sox5	In house (Figures S2C and S2D)	N/A
Goat anti-rabbit Alexa Fluor633 IgG	Invitrogen	Cat# A21070; *RRID*:AB_2535731
Goat anti-mouse Rhodamine Red IgG	Jackson Immunoresearch	Cat# 115-295-003; RRID:AB_2338756
Alexa Fluor488-conjugated streptavidin	Jackson Immunoresearch	Cat# 016-540-084; RRID:AB_2337249
Bacterial and Virus Strains		
AAV5-CaMKIIa-hChR2(H134)-EYFP	University of North Caroline (UNC Vector Core)	N/A
Chemicals, Peptides, and Recombinant Proteins		
Bisbenzimide H33258	Sigma-Aldrich	Cat# B2883; CAS: 23491-45-4
Neurobiotin tracer	Vector Labs	Cat# SP-1120
Experimental Models: Organisms/Strains		
Rat: Wistar	Instituto Cajal Animal facility	N/A
Rat: VGAT-VenusA	National Bioresource Project Japan. University of Kyoto	Cat#: 0554
Mouse: C57BL/6	Instituto Cajal Animal facility	N/A
Software and Algorithms		
MATLAB 2016b	Mathworks	https://www.mathworks.com
Ethovision v1.90	Noldus	http://www.noldus.com/animal-behavior-research/
ImageJ	NIH Image	https://imagej.net/ImageJ
Recording software	Molecular devices	ClampFit
MiniAnalysis Software v5	Synaptosoft	http://www.synaptosoft.com/MiniAnalysis/
NeuroExplorer v4.135	Nex Technologies	http://www.neuroexplorer.com/
Other		
Silicon probes: 16-channel linear; 100 μm inter-spacing; 413 μm2 electrode area	Neuronexus	A1x16-5mm-100-413
Silicon probes: 32-channel 2x16 linear; 100 μm inter-spacing; 413 μm2 electrode area; 200 μm inter-shank	Neuronexus	A2x16-10mm-200-413
Silicon probes: Prida 16ch-comb; 413 μm2 electrode area; 100 μm inter-shank	Neuronexus	A16x1-5mm-100-413
Tapered optic fibers	Optogenix	Lambda-B

CONTACT FOR REAGENT AND RESOURCE SHARING

Further information and requests for reagents and resources should be directed to and will be fulfilled by the Lead Contact, Dr. Liset M. de la Prida (lmprida@cajal.csic.es).

EXPERIMENTAL MODEL AND SUBJECT DETAILS

All protocols and procedures were performed according to the Spanish legislation (R.D. 1201/2005 and L.32/2007), the European Communities Council Directives of 1986 (86/609/EEC) and 2003 (2003/65/CE) for animal research, and were approved by the Ethics Committee of the Instituto Cajal (CSIC). Animals included in this study were not involved in any previous procedure, except for re-analysis of the large-scale datasets reported in Figure 6, which were published before (Oliva et al., 2016a, 2016b).

A total of 63 adult (150 –200 g) and 20 juvenile (50-70 g) male and female rats were used (both wild-type and VGAT-VenusA transgenic Wistar rats (Uematsu et al., 2008). For *in vivo* electrophysiological experiments, 10 wild-type adult rats both sexes were used for head-fixed recordings and 30 for urethane anesthetized experiments. For *in vitro* studies, 14 wild-type and 2 VGAT-VenusA juvenile rats were used. For histological studies, 6 VGAT-VenusA transgenic rats were used. For optogenetic experiments, we used 4 wild-type adult rats injected with AAV5-CamKII-ChR2. For behavioral assays, 2 wild-type and 11 VGAT-VenusA male rats were used. All rats were maintained in the animal facility of the Instituto Cajal, with water and food *ad libitum* in a 12 h light-dark cycle (7am to 7pm). In addition, we used 5 wild-type C57BL/6 mice and 1 Nestin-Cre/Sox5^fl/fl transgenic mouse for histological studies

METHOD DETAILS

Juxtacellular and LFP recordings in head-fixed rats

Rats were first implanted with fixation bars under isoflurane anesthesia (1.5%–2%) in oxygen (30%) while continuously monitored with an oximeter (MouseOx; Starr Life Sciences). After surgery, animals were habituated to head-fixed procedures (2-3 weeks habituation). The apparatus consisted in a cylindrical treadmill (40 cm diameter) adapted to a perforated table with a Narishige stereotaxic frame. The cylinder axle was equipped with a sensor to estimate speed and distance traveled analogically. The system was coupled to a water delivery pump controlled by a custom-made Arduino system. Animals learnt to run freely in the cylinder for water reward. After a couple of weeks of training, rats were able to stay confortable in the system for up to 2 hours with periods of RUN, immobility and sleep.

Once habituated to the apparatus, animals were anesthetized again with isoflurane to perform a craniotomy for electrophysiological recordings and stimulation (AP: −3.9 to −6 mm from Bregma; ML: 2-5 mm). A subcutaneous Ag/AgCl wire in the neck was implanted as reference and a bone screw served as ground. The craniotomy was sealed with sterile vaselyne and animals returned to their home cage. The day after, a bipolar tungsten wire was advanced to target CA3 while recording simultaneously from the contralateral CA1 with 16-ch silicon probes (NeuroNexus; 0.3–1.2 Mohm site impedance; 100 μm resolution; 177-413 μm^2 electrode area) at the contralateral CA1. Once the stimulation position was adjusted, the electrode was cemented and the craniotomy sealed again with vaselyne. The day after (2 days after surgery for craniotomy) single-cell and LFP recordings started.

For LFP recordings of CA2, we used either a 32-ch silicon probe consisting in 2 shanks of 16-channels linear arrays each separated 200 μm or single 16-channels linear arrays (100 μm resolution; 413 μm^2 electrode area). The angle of approach varies depending on alignment requirements with respect to the hippocampal curvature (typically from 0 to 30°). Penetrations were guided by characteristic response to cCA3 stimulation (Figure 1A; Figure S1). Then, single-cell recordings followed by juxtacellular labeling for post hoc immunohistochemical identification were obtained in combination with LFP. For juxtacellular recordings, a glass pipette (1.0mm x 0.58mm, ref 601000; A-M Systems) was filled with 1.5%–2.5% Neurobiotin in 0.5 M NaCl (impedance 8-15 MΩ). LFP signals were pre-amplified (4x gain) and recorded with a 32-channel AC amplifier (100x, Multichannel Systems) with analog filters (1Hz-5 kHz). Juxtacellular signals were acquired with an intracellular amplifier (Axoclamp 2B; Axon Instruments) at 100x gain. Single-cell and simultaneous LFP recordings were sampled at 20 kHz/channel with 12 bits precision (Digidata 1440; Molecular Devices).

After recording, cells were modulated using the juxtacellular labeling technique with positive current pulses (500-600 ms on-off pulses; 5-18 nA) while monitoring their response, as described before (Valero et al., 2015). One hour after, rats were perfused with 4% paraformaldehyde and the brain cut in 70 μm coronal sections. Labeled cells were identified using streptavidin-conjugated fluorophores and submitted to immunostaining studies. Only unambiguously identified cells are reported (3 cells were clearly identified out of 10 recorded cells).

Intracellular and LFP recordings under urethane

Rats were anesthetized (urethane 1.2 g/kg, i.p.), fastened to the stereotaxic frame and kept warmed (37° body temperature). Bilateral craniotomies were performed for stimulation (cCA3 at AP: −1.2 mm, ML: 2.9 mm; ipsilateral PP at AP: −7 mm; ML: 3.5 mm), and a window was drilled above the right hippocampus for recordings (AP: −3.7 mm; ML: 3 mm). The dura was gently removed and the *cisterna magna* opened and drained.

LFP recordings were guided by extracellular stimulation and electrophysiological hallmarks to target either CA1 or CA2 region (Figure S1). LFP signals were acquired as described before. Concentric bipolar electrodes were advanced 3.5 mm with 30° in the coronal plane to stimulate CA3 or 3 mm vertically to stimulate PP. Stimulation consisted of biphasic square pulses (0.2 ms duration, 0.05-1.2 mA every 5 s). A subcutaneous Ag/AgCl wire in the neck served as reference. Recording and stimulus position was confirmed by post hoc histological analysis.

For intracellular recording and labeling in current-clamp mode, sharp pipettes (1.5 mm/0.86 mm outer/inner diameter borosilicate glass; A-M Systems, Inc) were filled with 1.5 M potassium acetate and 2% Neurobiotin (Vector Labs, Inc; impedances: 50-100 MΩ). Signals were acquired with an intracellular amplifier (Axoclamp 900A, 100x gain). Before recordings started, the craniotomy was

covered by 3% agar to improve stability. The resting potential, input resistance and amplitude of action potentials was monitored all over experiments. After data collection, Neurobiotin was ejected using 500 ms depolarizing pulses at 0.5-2 nA at 1 Hz for 10-45 min. Rats were perfused with 4% paraformaldehyde and the brain cut in 70 μm coronal sections for posterior histological studies.

In vitro electrophysiology

Juvenile wild-type and VGAT-VenusA transgenic Wistar rats were used to prepare hippocampal slices, when PCP4 was already expressed (San Antonio et al., 2014). Animals were anesthetized with pentobarbital, intracardially perfused with cold 95% O_2 - 5% CO_2 artificial cerebrospinal fluid (ACSF; see below) and decapitated using approved procedures. Sagittal slices (400 μm) were prepared from the dorsal level of the hippocampus at 2-4 mm from midline using a Leica vibratome (Leica VT1200S). Slices were cut in a slicing ACSF whose composition was (in mM): 70 Sucrose, 86 NaCl, 2.5 KCl, 26 NaHCO3, 1 NaH2PO4, 0.5 CaCl2, 7 MgCl2, 25 glucose, pH 7.3 when balanced with 95% O_2 - 5% CO_2. After 15 min at 32°C, slices were transferred to a submerged holding chamber for at least 1hr at room temperature (RT) bathed with recording ACSF containing (in mM): 125 NaCl, 2.5 KCl, 26 NaHCO3, 1.25 NaH2PO4, 2.5 CaCl2, 1.3 MgCl2, 10 glucose, pH 7.3 when balanced with 95% O_2 - 5% CO_2.

For recording, slices were transferred to a submerged chamber continuously perfused with recording ACSF (2.5-3 ml/min) using a peristaltic pump (Gilson) and oxygen-impermeable Tygon tubes. Somatic patch-clamp recordings were obtained from neurons around the CA2 region under visual control with an upright microscope (BX51W, 60x lens; Olympus) at 32°C. Patch pipettes (pulled from borosilicate glass capillaries; World Precision Instruments, WPI) were filled with (in mM): 40 Cs-gluconate, 90 K-gluconate, 3 KCl, 1.5 NaCl, 1 MgCl2, 1 EGTA, 10 HEPES, 2 K2ATP, 0.3 NaGTP, 10 mM phosphocreatine and 0.1% Alexa568, pH 7.3 adjusted with KOH (osmolarity ∼300 mOsm). Electrodes filled with this solution had resistances of ∼4-6 MΩ.

Bipolar stimulating electrodes (tungsten wires, 0.5 mm separation, 0.5 MΩ, WPI) were positioned under visual control at the SP layer of CA3c/b or at the SLM layer of CA2. Extracellular field potentials were recorded with a patch-clamp pipette filled with ACSF coupled to one-channel AC amplifier (DAM-80; WPI). Stimulation intensity was adjusted homogenously between slices so that extracellular field potentials recorded at the CA1 or CA3 SR exhibited comparable responses (field EPSPs of 50-200 μV for 390-530 μA). In a subset of experiments, MF were stimulated at the tip of the upper DG blade, known to project to the CA3a-CA2 border specifically.

Whole-cell patch recordings were obtained in current- and voltage-clamp modes with an Axoclamp 2B and digitized at 20 kHz (Digidata 1440A; Molecular Devices). Pyramidal cells had stable resting potentials of at least −50 mV and access resistances lower than 25 MΩ. Capacitance compensation and bridge balance were performed for current-clamp recordings. The junction potential was not corrected. Thirty minutes after experiments, slices were fixed in 4% paraformaldehyde for histological studies.

Tissue processing and inmunohistochemistry

After completing experiments, animals were perfused with 4% paraformaldehyde and 15% saturated picric acid in 0.1 M, pH 7.4 phosphate buffered saline (PBS). Brains were postfixed overnight, washed in PBS and serially cut in 70 μm coronal sections (Leica VT 1000S vibratome). Sections containing the stimulus and probe tracks were identified with a stereomicroscope (S8APO, Leica). Sections containing Neurobiotin-labeled cells were localized by incubation in 1:400 Alexa Fluor488-conjugated streptavidin (Jackson ImmunoResearch 016-540-084) with 0.5% Triton X-100 in PBS (PBS-Tx) for 2 hours at RT. Slices recorded *in vitro* containing Alexa568 filled cells were fixed for 30 min, washed in PBS and processed similarly to others.

Sections containing the somata of recorded cells were treated with Triton 0.5% and 10% fetal bovine serum (FBS) in PBS. After washing, they were incubated overnight at RT with the primary antibody solution containing rabbit anti-calbindin (1:1000, CB D-28k, Swant CB-38), or mouse anti-calbindin (1:1000, CB D-28k, Swant 300) with 1% FBS in PBS-Tx to identify the MF. CB immunostaining was complemented with Wfs1 to identify CA1 pyramidal cells (1:1000, Proteintech 11558). For identifying the CA2 region, we used either rabbit anti-PCP4 (1:100, Sigma HPA005792) or mouse anti-α-Actinin2 (1:500;1:1000; Sigma A7811). CA3 pyramidal cells negative to Wfs1 and PCP4 were further examined for thorny excrescences. For Sox5 immunostaining we used an in-house developed polyclonal antibody (1:500; Figure S2D; Quiroga et al., 2015). After three washes in PBS-Tx, sections were incubated for 2 hours at RT with secondary antibodies: goat anti-rabbit Alexa Fluor633 (1:500, Invitrogen, A21070), and goat anti-mouse Alexa Fluor488 (Jackson Immunoresearch 115-545-003) or goat anti-mouse Rhodamine Red (1:200, Jackson ImmunoResearch, 115-295-003) in PBS-Tx-1%FBS. Following 10 min incubation with bisbenzimide H33258 (1:10000 in PBS, Sigma, B2883) for labeling nuclei, sections were washed and mounted on glass slides in Mowiol (17% polyvinyl alcohol 4-88, 33% glycerin and 2% thimerosal in PBS).

Multichannel fluorescence stacks were acquired with a confocal microscope (Leica SP5; LAS AF software v2.6.0) and the following channels (fluorophore, laser and excitation wavelength, emission spectral filter) were used: a) bisbenzimide, Diode 405 nm, 415–485 nm; b) Alexa Fluor488, Argon 488 nm, 499–535 nm; c) Rhodamine Red / Alexa Fluor568 / Texas Red, DPSS 561nm, 571–620 nm; d) Alexa Fluor633, HeNe 633 nm, 652–738 nm; and objectives HC PL APO CS 10.0x0.40 DRY UV, HCX PL APO lambda blue 20.0x0.70 IMM UV, HCX PL APO CS 40.0x1.25 OIL UV and HCX PL APO 63x IMM OIL. For illustration purposes, false colors were used.

All morphological analyses were performed blindly to electrophysiological data. The distance from the cell soma to the MF limit (taken as 0) or the cell position within SP (the superficial border taken at 0) was measured from confocal images using information from CB and bisbenzimide staining and the ImageJ software (NIH Image). The proximodistal distance to MF was measured along the linear SP contour.

Analysis of Sox5 expression

Immunohistochemical expression of Sox5 was analyzed both at the regional and single-cell levels. For regional analysis, Sox5 intensity was calculated from closed contours of 130 μm length delineated around the SP from the MF limits in the proximal and distal direction (mean of 2 confocal sections at 40x). Mean intensity was subtracted and normalized by the mean background signal taken from similar regions at SO, SR and SLM. Normalized intensity is represented as % (0% = background). Information from α-Actinin2 expression was used to identify CA2. Regional data from n = 5 sections from 4 rats was represented as a function of the distance to the MF border.

For single-cell analysis, the nucleus of α-Actinin2+ cells was delineated using bisbenzimide signal in one confocal optical section (7 sections from 4 rats). Only cells with the equator of their nuclei lying on the confocal plane were counted. For each cell, the distance to MF limit was measured. The mean Sox5 intensity per cell was calculated and normalized as before. Data was plotted as a function of the cell distance to MF. To evaluate expression trends, a Pearson correlation R-index was estimated for proximal and distal sectors separately in each section. The mean single-cell normalized intensity level was evaluated for proximal and distal α-Actinin2+ cells separately.

Optogenetics

To validate CA2 responses to electrical PP stimulation, we injected 2 wild-type Wistar rats with an adeno-associated virus (AAV5) carrying ChR2 under the control of CaMKII (AAV5-CamKII-ChR2) in the medial entorhinal cortex (Karl Deisseroth, UNC Vector Core). For stereotaxic surgery, rats were anesthetized with isoflurane (1.5%–2%) in oxygen (30%). Injections of 1μl at AP −9 mm and ML 5 mm (DV 4 mm) were made unilaterally to the site of recording (titer 4.6 10^{12} vg/ml). Rats recovered for 2-4 weeks to allow for adequately expression. For in vivo optogenetic experiments (n = 2 rats), light was delivered from a solid state blue laser (MBL-F-473, 300 mW maximal fiber output, CNI Laser, China) with Neuronexus opto-probes (flat optic fiber of 105 μm diameter mounted on 16-ch linear arrays) located stereoataxically at the angular bundle. LFP signals were recorded simultaneously from CA2 and CA1 layers with an independent probe. Laser stimulation ranged from 3-15 mW for short pulses of 2-5 ms. After experiments, animals were perfused with 4% paraformaldehyde and sagittal sections (70 μm) were obtained to validate infection. In vivo experiments (n = 2 rats), were performed similarly using an edged optical fiber (Optogenix; Italy). For in vitro experiments we used 16-channel silicon combs from Neuronexus (Prida design; interspaced 100 μm).

Analysis of LFP signals

Analysis of electrophysiological in vivo data was performed using routines written in MATLAB 7.10 (MathWorks). Multi-site LFPs from different layers were identified using characteristic physiological events, including sharp-wave ripples (to identify SR and SP) and maximal theta oscillations (for SLM). Characteristic evoked responses to contralateral CA3 and ipsilateral PP simulation were used to identify CA2 penetrations (Figure S1). One-dimensional current-source density (CSD) signals were calculated from the second spatial derivative of laminar LFPs (100 μm resolution). Smoothing was applied to CSD signals for visualization purposes only. Tissue conductivity was considered isotropic, and an arbitrary value of 1 was assigned to express CSD signal as mV/mm^2. In trying to handle with issues arising from the complex hippocampal geometry around CA2, we limited our intracellular-CSD analysis to penetrations going through distal CA2 (see Figure 4A inset). To avoid the CSD phase-reversal zone at the SR-SLM border, we chose SR sites at 100-200 μm from SP.

The power spectrum of LFP signals was estimated using the Fast Fourier transform (FFT). For theta activity, non-overlapping segments of continuous oscillations in the 4-12 Hz band were identified in LFP signals from SLM. The contribution of theta (4-12 Hz) and gamma (30-90 Hz) activity was evaluated from the spectral area at each oscillatory band using data from recording sites at SO, SP, SR and SLM. Gamma activity was separated in the lower (30-60 Hz) and high (60-90Hz) bands. We confirmed similar trends using detrended spectra. The location of probe penetrations along the SP was evaluated by estimating the linear distance to MF. Multiple probe penetrations were made per rat (typically 2 to 4). To reconstruct probe tracks reliably, relative stereotaxic coordinates and experimental history were documented.

For sharp-wave ripples, LFP recordings from SR were low-pass filtered at 100 Hz to identify sharp-waves and signals from SP were bandpass filtered between 100-600 Hz to identify ripples. We used forward-backward-zero-phase finite impulse response (FIR) filters of order 512 to preserve temporal relationships. For sharp-waves, filtered signals were smoothed (Gaussian kernel) and events detected by thresholding of > 3 SDs. For ripples, bandpass-filtered signals were smoothed (Savitzky-Golay) and events detected by thresholding of > 2 SDs. All pairs of detected events were visually confirmed. Time-frequency analysis of sharp-wave ripples was performed by applying multitaper spectral estimation in sliding windows with 97.7% overlap and frequency resolution of 10 Hz in the 90-600 Hz frequency range (only the 100-600 Hz range is shown) to data sweeps aligned by sharp-waves (±1sec). The time difference between the sharp-wave peak and the maximal ripple power was estimated and plotted as a function of the probe position with respect to MF.

Analysis of intracellular recordings

Passive electrophysiological properties (input resistance, membrane decay and capacitance) of neurons recorded intracellularly in vivo were measured using 500 ms currents step in current-clamp mode. Cells with intracellular action potential amplitude smaller than 40 mV were excluded. RMP and input resistance were estimated by linear regression between baseline potential data and the

associated holding current. Intrinsic firing properties, including action potential threshold, half-width duration and AHP were esti-mated from the first spike in response to depolarizing current pulses of 0.2 nA amplitude and 500 ms duration. The sag and maximal firing rate was calculated from current pulses of ± 0.3 nA amplitude. A bursting index was defined as the ratio of the number of com-plex spikes (minimum of 3 spikes < 8ms inter-spike interval) over the total number of spikes recorded during theta activity.

The power spectrum of intracellular membrane potential oscillations was calculated with FFT methods similar to LFP signals for different holding potentials. The contribution of theta (4-12 Hz) and gamma (30-90 Hz) bands was evaluated from the spectral ampli-tude of the FFT. We found comparable results by using the area below detrended power spectra. Pairwise theta coherence between the intracellular membrane potential and LFP or CSD signals was defined from the cross-spectral power densities at the peak fre-quency in the 4–12 Hz range at 1Hz resolution.

Phase-locking firing of single cells was measured from each spike using the Hilbert phase of theta peaks recorded at SLM. Each theta cycle was divided into 25 bins. Phase locking was quantified using the mean vector length (MVL) of phase distribution from 0 to 1. We also used a pairwise phase consistency measure (PPC) suitable for evaluating modulation of relatively small number of spikes (Vinck et al., 2012). The SLM theta trough was set at 0 and peaks at ± pi (or 180°). To establish links with previous data, we also estimated the corresponding theta peak at SP which exhibited a shift of −1.6 radians respect to the SLM trough due to theta wave asymmetries. To the purpose of this paper, this shift was not considered. Gamma modulation was evaluated similarly for LFP oscillations in the full gamma band (30-90 Hz) or in the slow (30-60Hz) and high (60-90 Hz) bands separately.

To evaluate theta rhythmicity of single-cell firing, we estimated the power spectrum of the autocorrelogram built at ± 0.5 s windows (1 ms bin size). A theta autocorrelation index was defined from the normalized area in the 4–12 Hz band. For visualization purposes, 45 bins were used to build autocorrelograms.

Analysis of juxtacellularly labeled cells

For juxtacellularly labeled cells, signals from glass pipettes were high-pass filtered at 300 Hz to detect positive spikes from the jux-tacellular recorded cell (> 8 SD). Simultaneous LFP signals at SLM and SP were processed similarly than for intracellular recordings. Interspike interval autocorrelograms (0.5 ms bins) were constructed using all detected spikes. The stability of the action potential waveform (peak-to-peak duration and amplitude as well as a spike asymmetry index defined as the ratio of the difference between the negative and positive baseline-to-peak amplitudes and their sum) was evaluated over the entire recording session (> 3 min), before juxtacellular electroporation. Baseline firing rate was stable for small movements of the pipette toward the cell, excluding me-chanical interferences. Phase-locking firing was evaluated similar as described for intracellular data.

Analysis of large-scale recordings of pyramidal cells during RUN and sleep

To test for functional proximodistal effects in large-scale simultaneous recordings of pyramidal cells from CA3, CA2 and CA1 regions we re-examined data by Oliva et al. (2016a, 2016b). This dataset comprised a total of 688 well isolated CA2 pyramidal cells recorded from 6 rats during spatial navigation in a linear maze and subsequent rapid-eye-movement (REM) sleep. Penetrations through CA2 was confirmed histologically and organized from proximal to distal positions (Figure 6A; Oliva et al., 2016b) and data organized as proximal (n = 387 pyramidal cells from 3 rats) and distal (n = 301 cells from 3 rats). In addition, parallel silicon shanks allowed isolation of 262 pyramidal cells from CA3a and 389 cells from the proximal CA1 region. Phase-locking firing to theta and gamma was analyzed as before using the SLM channel at CA1 as reference and quantified using the MVL. The SLM theta peak was set at 0 and troughs at ± pi (or 180°). Cross-correlation analysis was applied to quantify the degree of firing synchrony between CA3a, CA2 and CA1. To this purpose, the cross-correlation function was computed from the pyramidal cell population vector from each region in each rat separately in a window interval of ± 150ms. The spatial position of the rat during behavioral sessions allowed for examination of place field coding. Position and spiking data were binned in 5 cm pixels (Oliva et al., 2016a). A place field was defined as a continuous region (> 15 cm) with firing rate exceeding 10% of rate peak of > 2Hz and spatial coherence > 0.7 for cells with more than 50 spikes. Place cells were defined independent on direction in the linear maze. Place fields at the turning position in the track were not included in the analysis. Spatial information selectivity and sparsity were calculated using smoothed maps of spike and occupancy (Gaussian kernel of 5 cm).

QUANTIFICATION AND STATISTICAL ANALYSIS

Statistical analysis was performed with MATLAB. No statistical method was used to predetermine sample sizes, which were similar to those reported in similar reports (Valero et al., 2015). Normality and homoscedasticity were evaluated with the Kolmogorov–Smirnov and Levene's tests, respectively. The exact number of replications for each experiment is detailed in text and figures.

One-way ANOVAs or Kruskal-Wallis tests were applied for cell-types or regions. Post hoc comparisons were evaluated with either the Tukey-Kramer or Wilcoxon tests. Proximodistal and deep-superficial trends were evaluated with the Pearson product-moment correlation coefficient, which was tested against 0 (i.e., no correlation was the null hypothesis) at $p < 0.05$ (two sided). Both the Pearson coefficient and p value are reported to facilitate interpretation.

To account for mixed statistical effects on measurements of interest, a generalized linear model (GLM) was implemented as a linear combination of the following variables: cell-type, distance to MF and distance within SP. The impact of each variable in the GLM

model was then tested with ANOVA and the p value reported after Tukey-Kramer posthoc correction. Variables having a significant impact in explaining the measurement of interest show p values < 0.05.

DATA AND SOFTWARE AVAILABILITY

Freely available software and algorithms used for analysis are listed in the Key Resources Table. Some analyses were specifically designed for the purpose of this paper using routines written in MATLAB 7.10 (MathWorks). All custom scripts and data contained in this manuscript are available upon request from the Lead Contact.

Supplemental Information

Proximodistal Organization

of the CA2 Hippocampal Area

Ivan Fernandez-Lamo, Daniel Gomez-Dominguez, Alberto Sanchez-Aguilera, Azahara Oliva, Aixa Victoria Morales, Manuel Valero, Elena Cid, Antal Berenyi, and Liset Menendez de la Prida
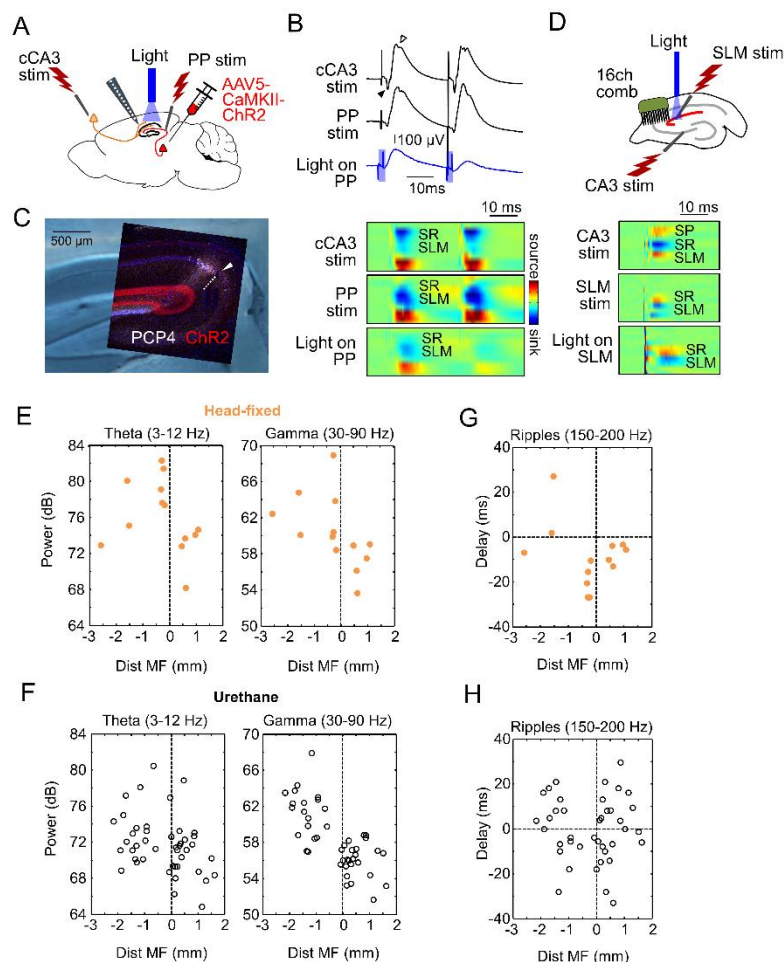
Figure S1. Electrophysiological features around CA2. Related to Figure 1.

(A) The CA2 region was targeted in vivo guided by spontaneous LFP signals and characteristic responses to stimulation of both the contralateral CA3 (cCA3) and perforant pathway (PP). The probe position was histologically validated after experiments. In a subset of animals, we used optogenetics to validate CA2 responses to PP stimulation. To this purpose, rats were injected with AAV5-CaMKII-ChR2 in the medial entorhinal cortex 3 weeks before experiments.

(B) In the SP of CA2, cCA3 stimulation elicited an antidromic spike (black arrowhead) followed by an orthodromic spike of variable amplitude (open arrowhead). PP electrical stimulation evoked a clear synaptic event typically associated to a small orthodromic response. These two characteristics aided us in targeting CA2 precisely. Optogenetic stimulation of entorhinal inputs elicited similar synaptic responses in CA2 than PP electrical stimulation, but the orthodromic spike was less reliably elicited. Current source density (CSD) signals are shown below traces. Note similar CSD sinks at SLM after electrical and optical stimulation of entorhinal terminals. All data from the same rat.

(C) Histological validation of the experiment shown in B. The CA2 region was identified with immunostaining for PCP4. Note the probe track indicated (discontinuous line and arrowhead). ChR2 was expressed both in layers II and III of the entorhinal cortex, but only ECII stellate cell terminals project to CA2.

(D) In vitro recordings to validate CA2 responses to SLM stimulation in one rat injected with AAV5-CaMKII-ChR2 in the medial entorhinal cortex. A 16-channel silicon comb was used to record laminar signals. The CSD profile is shown at bottom. Note similar CSD responses to electrical and optical stimulation of the entorhinal terminals at SLM.

(E) Individual spectral area of the theta (3-12 Hz) and gamma bands (30-90 Hz) plotted as a function of electrode distance to MF as measured in head-fixed conditions. Data from n=12 recordings from n=5 drug-free rats.

(F) Same for data obtained under urethane (52 recording locations from n=30 urethane anesthetized rats).

(G) Delay between the ripple and SPW peaks as a function of recording location. Data from n=13 recordings from n=5 drug-free rats.

(H) Same for data obtained under urethane (52 recording locations from n=30 urethane anesthetized rats)
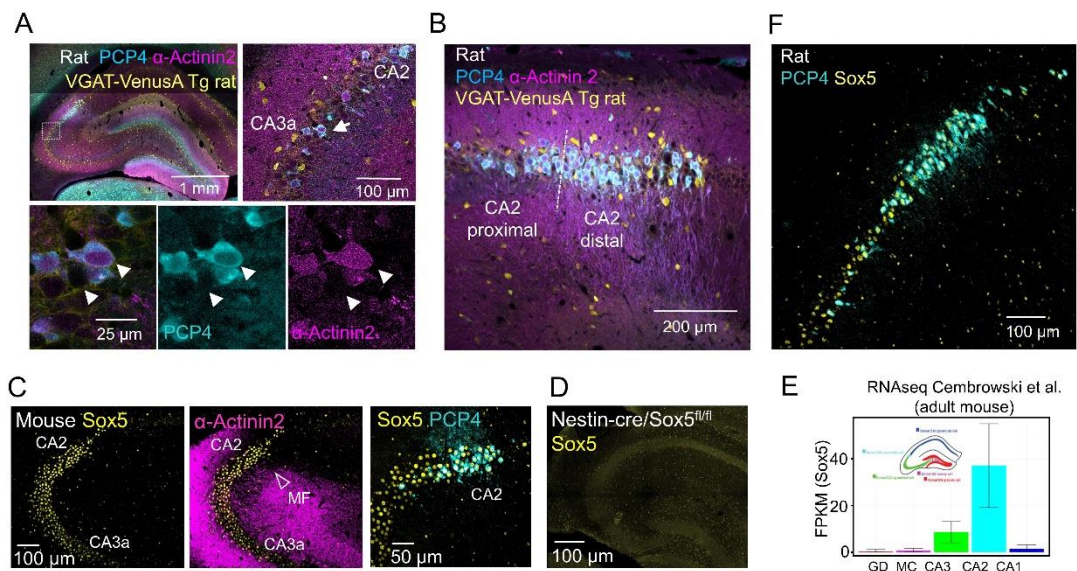
Figure S2. Proximodistal heterogeneity around CA2. Related to Figure 2.

(A) Double immunostaining against α-Actinin2 and PCP4 as evaluated in coronal sections from VGAT-VenusA transgenic rats. α-Actinin2 and PCP4 co-localized in CA2 pyramidal cells. Note some PCP4+ cells dispersed in CA3a (enlarged box shown at right). Bottom images show details of a PCP4+ and a PCP4- cell from CA3a that differ in their intensity of α-Actinin2 signal.

(B) Co-localization between α-Actinin2 and PCP4 in the CA2 region (one confocal optical section from a VGAT-VenusA rat).

(C) Immunohistochemical expression of Sox5 in a representative section from an adult mouse (one confocal section) co-localized with α-Actinin2 and PCP4. In mouse α-Actinin2 is mildly expressed at the somata.

(D) Validation of the rabbit Sox5 polyclonal antibody tested in a brain coronal section from a Nestin-cre/Sox5$^{fl/fl}$ mutant mouse.

(E) Quantitative regional RNAseq data from Hipposeq (Cembrowski et al., 2016).

(F) Co-localization between PCP4 and Sox5 in rat.

Table S1. Intrinsic properties of single cells recorded in vivo. Related to Figure 2.

|	PCP4-/Thorn n=5	PCP4+ n=10	Wfs1+ n=9	GLM (P-value)			
				Cell-type	Distance to MF	Distance to SR	All factors
Resting potential (mV)	-59.7 ± 3.4	-58.7 ± 4.2	-60.5 ± 5.9	0.7124	0.2373	0.9689	0.4855
Input resistance (MΩ)	20.1 ± 11.1	20.4 ± 9.5	36.3 ± 16.2	**0.0249**	**0.0185**	0.2510	**0.0246**
Membrane time constant (ms)	8.9 ± 4.2	6.6 ± 5.5	10.9 ± 3.8	0.1782	0.2214	0.4262	0.2859
Sag amplitude @-0.3nA (mV)	0.59 ± 0.27	1.08 ± 0.51	1.08 ± 0.47	0.1327	**0.0421**	0.2430	**0.0494**
Max firing rate @0.3nA (Hz)	5.7 ± 2.4	7.8 ± 4.1	20.4 ± 10.1	**0.0006**	**0.0006**	0.8055	**0.0021**
Firing rate adapt @0.3nA	0.52 ± 0.08	0.63 ± 0.02	0.65 ± 0.04	**0.0018**	**0.0205**	0.5592	0.0514
Bursting Index	0.10 ± 0.20	0.08 ± 0.18	0.046 ± 0.09	0.7902	0.4792	0.6983	0.6870
AP threshold (mV)	-53.5 ± 4.2	-49.5 ± 3.2	-48.1 ± 4.4	0.0632	0.0520	0.5128	0.1360
AP half-width (ms)	0.94 ± 0.13	0.93 ± 0.14	0.95 ± 0.16	0.9310	0.9362	0.8130	0.9706
AHP amp (mV)	2.9 ± 1.5	3.4 ± 1.6	5.4 ± 1.8	**0.0182**	**0.0106**	0.1959	**0.0254**
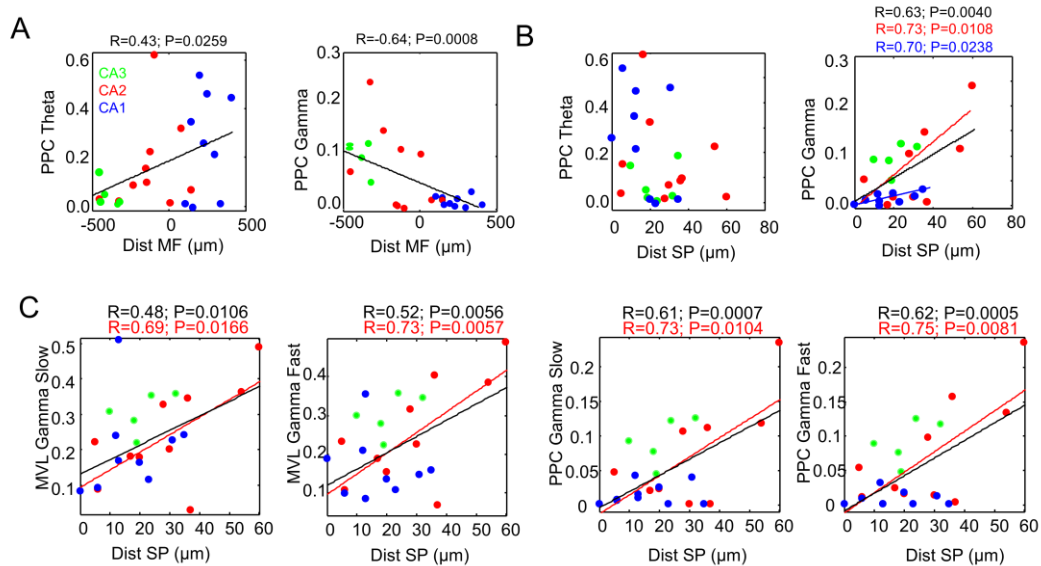
Figure S3. Phase locked firing of morphologically identified single cells. Related to Figure 3.

(A) Modulation strength calculated from the PPC index.
(B) Distribution of the PPC modulation strength as a function of the cell distance within SP. Note strong deep-superficial trends for gamma activity within the CA2 and CA1 subgroups, and for all grups together. The SP border with SP is at 0 (superficial).
(C) Modulation strength during slow and fast gamma activities as a function of the deep-superficial location of recorded cells.

Table S2. Theta and gamma modulation of single cells recorded in vivo. Related to Figure 3

| | PCP4-/Thorny n=5 | PCP4+ n=10 | Wfs1+ n=9 | GLM (P-value) | | | |
				Cell-type	Dist to MF	Dist to SR	All factors
All cells in the database							
Theta autocorrelation index	0.38 ± 0.03	0.38 ± 0.07	0.36 ± 0.05	0.4785	0.11611	**0.00328**	**0.00756**
Theta index (MVL)	0.17 ± 0.13	0.29 ± 0.16	0.45 ± 0.27	**0.0201**	**0.01528**	0.27042	**0.02176**
Gamma index (MVL)	0.30 ± 0.09	0.24 ± 0.13	0.18 ± 0.09	0.2708	**0.04298**	**0.00761**	**0.00313**
Theta phase (rad)	1.80 ± 0.91	0.45 ± 1.07	-2.56 ± 0.72	**<0.0001**	**<0.0001**	**0.0389**	**<0.0001**
Gamma phase (rad)	3.09 ± 0.53	2.76 ± 1.03	2.74 ± 1.01	0.8737	0.6495	0.1145	0.2266
Theta phase (deg)	103.3 ± 52.2	140.2 ± 61.2	-126.9 ± 1.03	**<0.0001**	**<0.0001**	**0.0389**	**<0.0001**
Gamma phase (deg)	177.4 ± 30.5	158.4 ± 58.6	157.1 ± 57.9	0.8737	0.6495	0.1145	0.2266
Theta index (PPC)	0.04 ± 0.06	0.16 ± 0.18	0.25 ± 0.21	0.1477	**0.04250**	0.18519	**0.04060**
Gamma index (PPC)	0.091 ± 0.026	0.067 ± 0.075	0.0108 ± 0.009	**0.0265**	**<0.0001**	**<0.0001**	**<0.0001**
Only cells recorded against CA1 LFP							
	PCP4-/Thorny n=4	PCP4+ n=5	Wfs1+ n=8	Cell-type	Dist to MF	Dist to SR	All factors
Theta autocorrelation index	0.38 ± 0.03	0.41 ± 0.08	0.35 ± 0.05	0.3223	0.1767	**0.0413**	0.0681
Theta index (MVL)	0.16 ± 0.15	0.28 ± 0.19	0.41 ± 0.26	0.2109	**0.0383**	0.1391	**0.0373**
Gamma index (MVL)	0.30 ± 0.06	0.25 ± 0.16	0.19 ± 0.09	0.2516	0.0506	**0.0017**	**0.0016**
Theta phase (rad)	2.07 ± 0.95	1.89 ± 1.06	-2.76 ± 0.75	**<0.0001**	**<0.0001**	0.0664	**<0.0001**
Gamma phase (rad)	-3.08 ± 0.56	2.76 ± 0.74	2.56 ± 1.04	0.4633	0.4222	0.0669	0.1196
Theta phase (deg)	118.6 ± 54.6	108.6 ± 60.9	-150.3 ± 42.8	**<0.0001**	**<0.0001**	0.0664	**<0.0001**
Gamma phase (deg)	-176.9 ± 32.3	158.2 ± 42.3	147.1 ± 59.5	0.4633	0.4222	0.0669	0.1196
Theta index (PPC)	0.04 ± 0.06	0.11 ± 0.13	0.21 ± 0.19	0.2108	**0.0345**	0.2350	**0.0480**
Gamma index (PPC)	0.093 ± 0.034	0.081 ± 0.096	-0.005 ± 0.038	**0.0237**	**<0.0001**	**<0.0001**	**<0.0001**
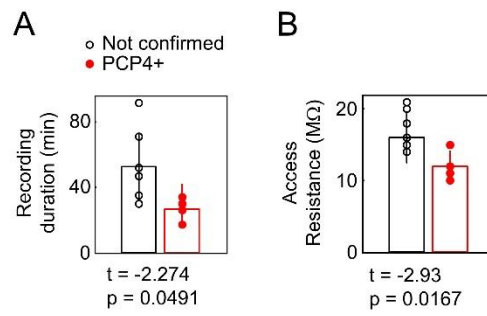
Figure S4. Effect of cell dialysis on immunoreactivity to PCP4. Related to Figure 5.

(A) Significant difference of recording duration of PCP4+ cells versus cells with non-confirmed immunoreactivity suggest dialyzing of cytoplasmic content is a major factor against neurochemical confirmation of CA2 cells with whole-cell patch recordings in vitro. Data from n=7 not confirmed cells, n=4 PCP4+ CA2 pyramidal cells. Results from a Student t-test are shown at bottom.
(B) Significant difference of access resistance through the patch pipette in PCP4+ cells versus cells with non-confirmed immunoreactivity.
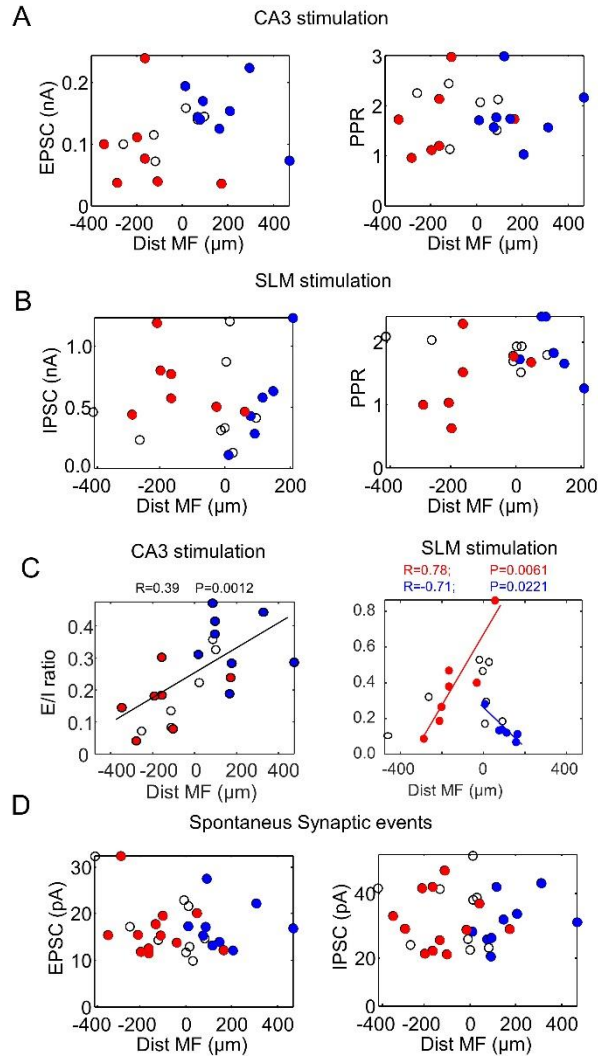
Figure S5. Synaptic activity of CA2 pyramidal cells recorded in vitro. Related to Figure 5.

(A) Relationship between the amplitude of the CA3-evoked EPSCs and paired-pulse ration (PPR) with the distance to MF. Cells without thorny excrescences and not confirmed with PCP4 (red) or Wfs1 (blue) immunostaining are shown in black. Data from n=6 not-confirmed cells, n=7 PCP4+ CA2 pyramidal cells and n=8 Wfs1+ CA1 pyramidal cells.
(B) Proximodistal distribution of the amplitude of SLM-evoked IPSCs and PPR. Data from n=6 not-confirmed cells, n=7 PCP4+ CA2 pyramidal cells and n=6 Wfs1+ CA1 pyramidal cells.
(C) E/I and I/E ratio for CA3 and SLM stimulation.
(D) Distribution of the amplitude of spontaneous EPSCs and IPSCs with the cell proximo-distal position. Data from n=9 not-confirmed cells, n=12 PCP4+ CA2 pyramidal cells and n=9 Wfs1+ CA1 pyramidal cells.
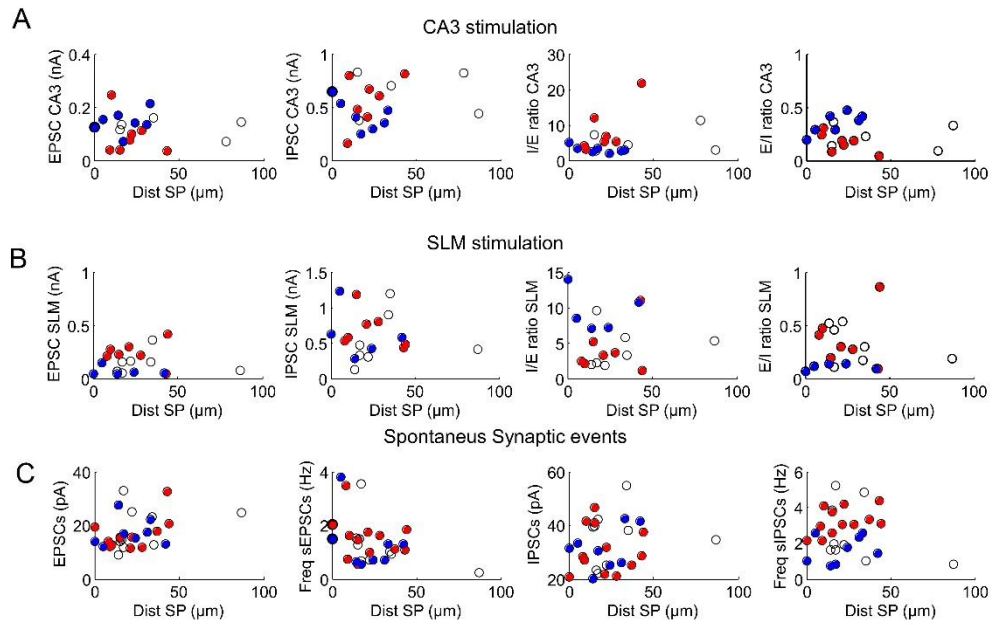
Figure S6. Relationship between synaptic currents and the cell location within SP (deep-superficial axis). Related to Figure 5.

(A) Individual data for synaptic currents evoked by CA3 stimulation plotted as a function of cell location within the SP layer. Same data as before.
(B) Same for synaptic currents evoked by stimulation at the SLM layer.
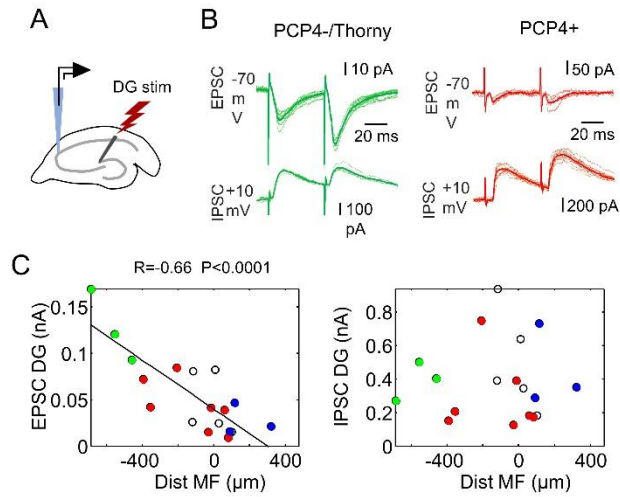(C) Same for the amplitude and frequency of spontaneous events.

Figure S7. Responses to MF stimulation. Related to Figure 5.

(A) MF were stimulated at the upper blade tip of the DG.
(B) Examples of a CA3 and CA2 pyramidal cell repsonses to MF stimulation.
(C) Individual data for synaptic currents evoked by MF stimulation plotted as a function of the proximodistal cell location. Data from n=3 CA3a pyramidal cells, n=7 PCP4+ CA2 cells and n=3 Wfs1+ CA1 cell. In n=4 cells immunoreactivity to Wfs1 and PCP4+ was not confirmed (no thorny excrescences).